# Advances in hydrogel-based photothermal interfacial solar steam generation: classifications, mechanisms, and applications

Yongqian Cui, Xinxin Liang, Ying Wang, Jingyi Wang, Jenyuk Lohwacharin, Eric Lichtfouse, Chuanyi Wang

Advanced Functional Material 2025, 2509130. https://doi.org/10.1002/adfm.202509130

# Advances in Hydrogel-Based Photothermal Interfacial Solar Steam Generation: Classifications, Mechanisms, and Applications

*Yongqian Cui, Xinxin Liang, Ying Wang, Jingyi Wang, Jenyuk Lohwacharin, Eric Lichtfouse, and Chuanyi Wang**

**The growing global demand for freshwater has driven considerable attention toward photothermal interfacial solar steam generation (PISSG), where hydrogels are widely used due to their excellent water absorption, efficient environmental friendliness, and favorable interface properties. However, recent review mostly focuses on photothermal materials' design and the mechanisms for reducing evaporation enthalpy, with limited discussion on diverse substrates, physicochemical properties of hydrogels, and thermodynamic analysis during the PISSG. This work aims to systematically review the current progress of hydrogel-based PISSG and the challenges in practical applications. It begins with the classification of hydrogels on different substrates, mainly including cellulose, polyvinyl alcohol, polyacrylamide, and sodium alginate. Subsequently, the properties of hydrogels, photothermal conversion mechanism, and thermodynamics of interfacial evaporation are highlighted to illustrate how hydrogels optimize PISSG. Furthermore, the practical applications, ranging from seawater desalination, wastewater purification, photocatalytic degradation, multiple energy harvesting and conversion, and sterilization are broadly presented. Finally, the future research directions are proposed. Through this review, a comprehensive understanding of hydrogel-based evaporators in PISSG is proposed to address potential issues in both fundamental research and practical applications, thereby contributing to the resolution of global water scarcity challenges.**

## 1. Introduction

The Earth possesses an estimated 1.386 billion cubic kilometers of water resources in total. However, over 97% is brackish water. Among the remaining freshwater reserves, more than two-thirds (68%) remain locked in polar ice caps and glaciers. The underground reserves constitute the remaining 30% of the world's freshwater supply. In contrast, surface freshwater sources, including rivers and lakes, represent merely 93 100 cubic kilometers, which is a mere 1/15 000th of the overall freshwater volume (**Figure 1**). Nonetheless, rivers and lakes continue to serve as the primary sources of water for individuals, and the lack of accessible drinking water resources is a serious issue.[1] Approximately 29% of the world's population lacks access to clean and safe drinking water, and 6% of deaths in economically stressed countries are caused by consuming unsafe water.[2] By 2050, nearly half of the world's population is expected to encounter varying degrees of water scarcity, which could greatly impact people's everyday lives. The availability of fresh water is facing growing threats from a combination of factors, including climate change, rapid urban expansion, and the unsustainable exploitation of water resources, all of which significantly diminish water supplies.[3] The urgent need for an innovative and sustainable approach to water treatment is more pressing than ever.[4]

Currently, there are two primary approaches for desalinating seawater. The first one utilizes filtration techniques, exemplified

Y. Cui, X. Liang, Y. Wang, J. Wang, C. Wang
School of Environmental Science and Engineering
Shaanxi University of Science and Technology
Xian 710021, P. R. China
E-mail: wangchuanyi@sust.edu.cn
C. Wang
Jiangxi Key Lab of Flexible Electronics
Flexible Electronics Innovation Institute
Jiangxi Science and Technology Normal University
Nanchang, Jiangxi 330013, P. R. China
E. Lichtfouse
State Key Laboratory of Multiphase Flow in Power Engineering
Xi'an Jiaotong University
Xi'an, Shaanxi 710049, China
J. Lohwacharin
Department of Environmental and Sustainable Engineering
Faculty of Engineering
Chulalongkorn University
254 Phayathai Road, Pathumwan, Bangkok 10330, Thailand

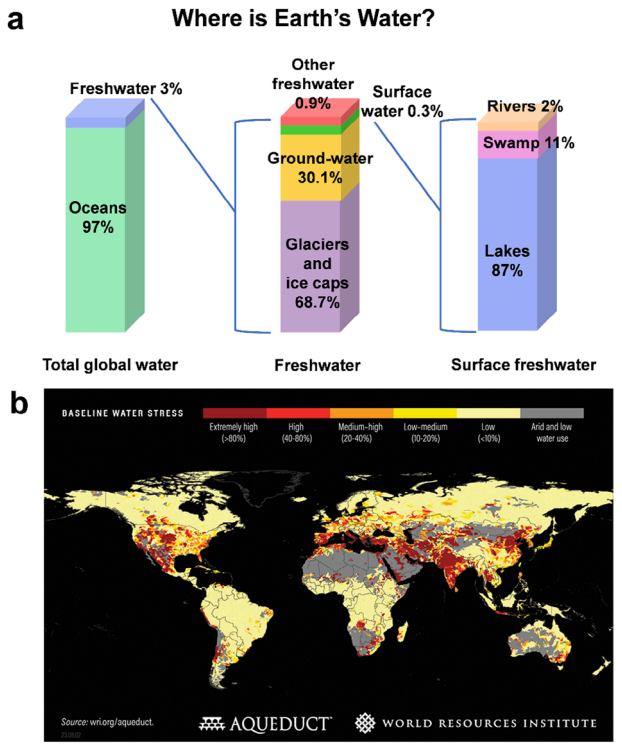


**Figure 1.** a) Distribution of Earth's water (source: water.usgs.gov). b) Global water stress (source: wri.org/aqueduct).

by seawater reverse osmosis.[5] The second one relies on thermal processes that convert water into steam, effectively separating heavy metal ions and other impurities.[6] Nonetheless, both of these approaches for extracting fresh water from seawater require large equipment and significant consumption of electricity, particularly when powered by fossil fuels. Consequently, there has been significant interest in utilizing solar energy for interfacial evaporation, a process referred to as photothermal interfacial solar steam generation (PISSG), which is not only cost-effective but also environmentally sustainable, providing a viable alternative to address our current water needs.[7]

In contrast to conventional solar-driven steam generation systems, which rely on bottom-generated heat to vaporize the upper layer of water (**Figure 2a**), solar-driven photothermal evaporation undergoes a distinct approach known as nanofluid solar heating. This technique utilizes dispersed photothermal materials with enhanced broadband light absorption capabilities to directly heat the entire water volume (Figure 2b). Simultaneously, the produced steam traverses the bulk liquid before reaching the air-water interface for vapor release, which results in significant energy loss to the bulk water, ultimately reducing the efficiency of solar-to-steam conversion. To further improve energy efficiency, PISSG has been introduced (Figure 2c).[8] These systems employ photothermal materials that remain on the water's surface, converting absorbed solar energy into heat, which facilitates direct evaporation at the water-air interface. To minimize heat conduction losses to the water beneath, a thermal insulation layer is commonly in the supporting substrate. This design helps to retain the generated heat at the photothermal surface, thereby expediting the vaporization of water and substantially increasing the efficiency of solar-to-steam conversion.

The mechanism of PISSG relies on light absorption and photothermal conversion performance of solar photothermal agents, which is satisfied by harnessing solar energy and converting it into thermal energy via a photothermal material (Figure 2d,e).[9] Optimized water supply and transport channels ensure sufficient water contact on the surface of the photothermal interface.[10] In general, to meet the two basic requirements for a desired evaporation rate (ER), photothermal conversion materials are commonly integrated into porous substrates such as aerogels, hydrogels, sponges, and fabrics.[11] Among these, the hydrogel-based photothermal evaporator has garnered significant attention owing to its various advantages, including sample preparation, low cost, strong scalability, and eco-friendliness.[1b] Initially, during the process of PISSG, hydrogels possess the capability to rapidly absorb and retain substantial quantities of water, which enables them to function as an effective reservoir, significantly enhancing their efficiency as water evaporation media (low water evaporation enthalpy).[12] By modulating the structure and composition of hydrogels, their capability to absorb sunlight can be significantly improved, which not only boosts photothermal conversion efficiency but also enhances the performance of hydrogels in light-driven evaporation applications. Second, the environmentally friendly properties of hydrogels make their application in the utilization of renewable resources more attractive compared to traditional materials.[13] Hydrogels are generally composed of natural polymers or biocompatible materials that are biodegradable and have a low environmental impact.[14] Specifically, biodegradability means that the hydrogel is biodegraded through enzymatic hydrolysis and microbial degradation of natural polysaccharides, producing safe and non-toxic degradation products.[15] Furthermore, its biodegradability offsets the energy costs of its synthesis, further confirming its eco-friendliness.

In recent years, many efforts have been directed at the advancements of hydrogel applications in PISSG (Figure 2f). An in-depth review conducted by Zhao et al. surveyed the mechanisms by which hydrogel solar evaporators reduce evaporation enthalpy.[16] Sharshir and colleagues examined the progress in photothermal hydrogel-based materials designed for water evaporation, water purification, and wastewater treatment, and contrasted these innovations with conventional materials.[17] Nonetheless, this review was published in 2020, which is over 5 years ago. Since then, notable progress has emerged, concentrating on hydrogel-based solar interface evaporators aimed at seawater desalination. Yu et al. provided a comprehensive review of the latest advancements in hydrogel-based evaporators for solar water purification, covering aspects such as material selection, molecular engineering, and structural design.[18] However, existing reviews offer limited discussion on the diverse substrates, physicochemical properties of hydrogels, and thermodynamic analysis during the interfacial evaporation process. From this prospect, this review first introduces different hydrogels on different substrates. Second, the physicochemical properties of hydrogels affecting PISSG performance, the photothermal conversion mechanism, as well as thermodynamics and interfacial evaporation will be discussed. Subsequently, various practical applications, including seawater desalination, wastewater purification, photocatalytic degradation, multiple energy harvesting and conversion, and sterilization will

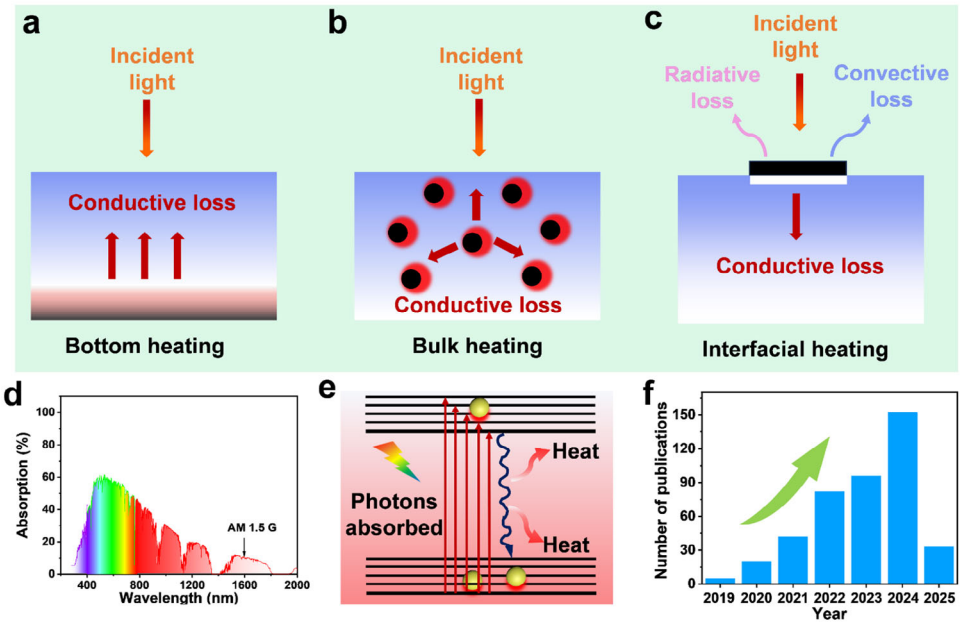


**Figure 2.** Energy nexus during a) bottom heating, b) bulk heating, and c) interfacial heating solar steam generation processes. d) UV-Vis-NIR absorption spectrum of AM 1.5G. e) Schematic diagram of photothermal conversion. f) The number of publications searched on WOS for "hydrogel evaporator".

be discussed (**Figure 3**). Finally, the challenges and prospects associated with photothermal hydrogel-based solar-driven interface evaporators and future development trends are analyzed and summarized.

## 2. The Classification of Hydrogels on Different Substrates

Hydrogels are 3D networks that are highly hydrated and crosslinked, and they may consist of a diverse array of chemical components and structural charges.[7a] The hydrogel framework is formed from hydrophilic groups such as -OH, -COOH, $-NH_2$, $-CONH_2$, and $-SO_3H$, or created through hydrated polymer networks in aqueous environments. The incorporation of these groups is a significant factor contributing to the favorable hydrophilicity of hydrogels. The properties of hydrogel surfaces are predominantly shaped by their functional groups, surface morphology, and overall network structure. These hydrogels have the potential to either stabilize reinforcing agents within the aqueous precursor solution, which in turn promotes an even distribution of catalysts throughout the hydrophilic matrix, or engage with other components of the gel through various interactions, such as electrostatic forces, hydrogen bonding, or other mechanisms. Due to their ability to interact with various functional groups, such as covalent, ionic, and hydrogen bonds, hydrogels have increasingly garnered interest in fields that require polymers with unique characteristics. Simultaneously, due to their porous structures, hydrogels are predominantly utilized for applications such as PISSG (**Table 1**).

Synthetic hydrogel materials are vital to the advancement of hydrogel technologies. Hydrogels, which are widely used in PISSG, can be categorized based on the types of synthetic materials into these groups: namely, cellulose-based, polyvinyl alcohol (PVA)-based, polyacrylamide (PAM)-based, sodium alginate (SA)-based and other hydrogels.

### 2.1. Cellulose-Based Hydrogels

Cellulose, a globally abundant and sustainable natural polymer, represents an almost limitless and eco-friendly raw material extensively utilized in PISSG applications.[53] The presence of numerous -OH groups in cellulose enables the formation of hydrogels through either physical or chemical crosslinking. A straightforward one-step method has been established for synthesizing hydrogel from unsubstituted cellulose in a NaOH/urea aqueous solution, employing epichlorohydrin as a crosslinking agent. This approach offers a quick and efficient means of preparing environmentally friendly hydrogels derived from unsubstituted cellulose.

Wang and colleagues developed a dual-layer cellulose hydrogel (DCH) for solar steam generation in the process of seawater desalination (**Figure 4a**).[26] Under one sun irradiation, the average ER and the steam generation efficiency reach 1.582 kg $m^{-2}$ $h^{-1}$ and 91.4%, respectively (Figure 4b,c). This sets the stage for cellulose-based hydrogels to emerge as a biodegradable, cost-effective, and environmentally friendly option for solar steam generation. Liu and his colleagues developed a 3D hierarchically porous hydrogel composed of cellulose, alginate, and carbon black. This innovative evaporator demonstrated an impressive ER of 1.33 kg $m^{-2}$ $h^{-1}$ and achieved a solar energy conversion efficiency of 90.6% under one sun irradiation, indicating great application prospects in seawater desalination and wastewater purification (Figure 4d–f).[24] Qin et al. used lignocellulose as the substrate to prepare a hydrogel evaporator, which achieved an ER of 1.83 kg $m^{-2}$ $h^{-1}$ and a photothermal conversion efficiency of 86.5% under one sun, respectively.[22] Simultaneously, the

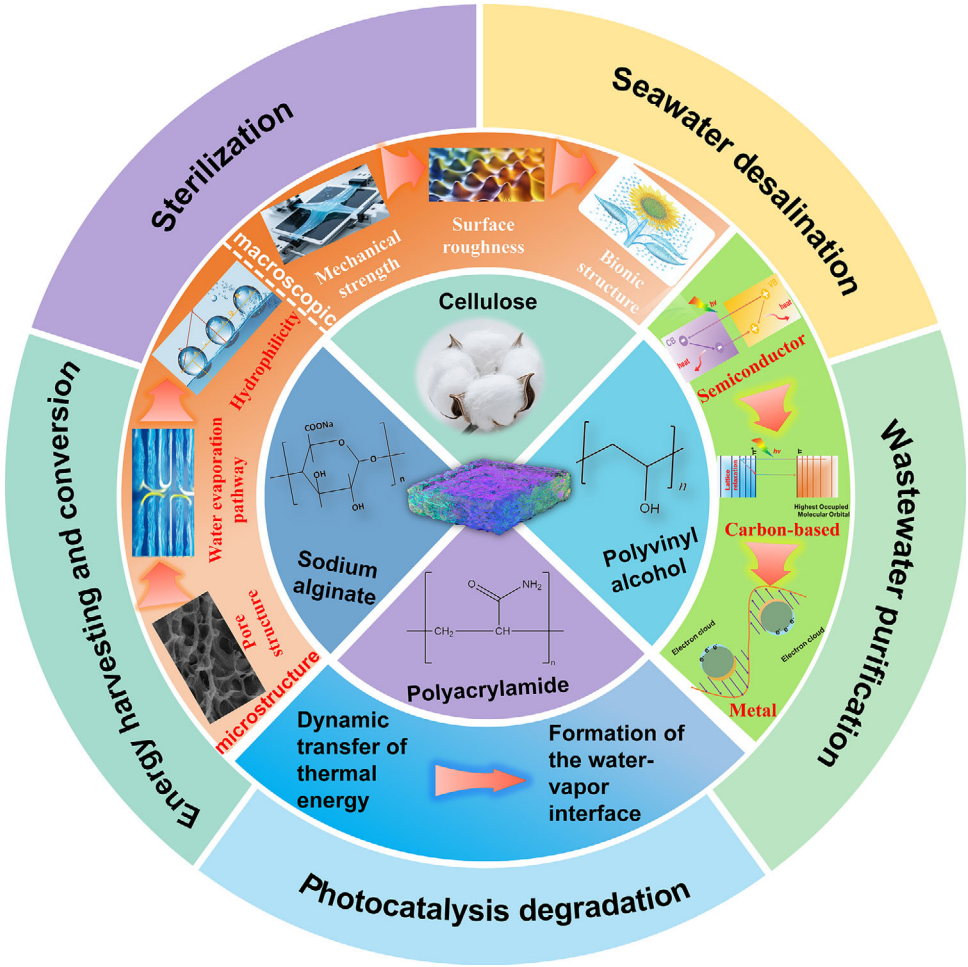


**Figure 3.** An overview of hydrogel-based evaporators including different substrates, properties, photothermal conversion mechanisms, thermodynamics and interfacial evaporation, and various applications.

evaporator has the capability to remove more than 99.95% of primary metal ions from seawater, resulting in the production of freshwater. This research highlights an environmentally sustainable and cost-effective approach for the continuous generation of freshwater from seawater, utilizing a hydrogel evaporator that is entirely derived from lignocellulosic biomass. Yao et al. developed a solar steam evaporator by incorporating a copper sulfide (CuS) semiconductor into cellulose hydrogel.[54] When subjected to one sun irradiation, the optimized rates of evaporation and solar-to-steam efficiency can achieve impressive values of 2.2 kg $m^{-2}$ $h^{-1}$ and 87%, respectively. The excellent ER is due to the hydrophilicity of the cellulose framework, which ensures a sufficient supply of water and exhibits a low enthalpy of water evaporation. Such a functional hydrogel evaporator holds great potential for practical water treatment and solar-driven applications.

Cellulose, a natural polymer material, possesses renewability and aligns with the principles of green sustainable development. Its high hydrophilicity allows it to absorb substantial amounts of water, and its porous structure facilitates the transport and diffusion of steam. Through the rational construction of cellulose-based hydrogels, the efficiency of steam generation can be improved, driving the advancement of related applications.

### 2.2. Polyvinyl Alcohol-Based Hydrogels

PVA is an important synthetic polymer material widely utilized in the synthesis of hydrogels due to its excellent solubility in water, allowing it to form transparent and flexible films.[55] PVA hydrogels can typically be prepared through various methods, including physical crosslinking, chemical crosslinking, and physicochemical crosslinking.[37] The prepared PVA hydrogels, which possess high water content, can provide the necessary water source for evaporation. Furthermore, the porous structure of PVA hydrogels exhibits good permeability, allowing steam to pass through smoothly and thereby increasing the efficiency of steam generation, which is particularly crucial for regulating moisture evaporation during the interfacial evaporation process of PVA hydrogels.[56] Additionally, the surface of PVA hydrogels can be modified using physical or chemical methods to enhance hydrophobicity or hydrophilicity, thereby effectively controlling the rate of steam generation.[57] As a biodegradable polymer, PVA has

**Table 1.** PISSG performance versus different hydrogel types of synthetic materials.

| Different substrates | Evaporators | Cross-linking methods | ER [Kg $m^{-2}$ $h^{-1}$] one sun | Efficiency [%] | Refs. |
|---|---|---|---|---|---|
| Cellulose-based hydrogels | polyaniline cellulose hydrogel | chemical | 3.02 | 89.09 | [19] |
| | 0D sulfhydryl-based hydrogel | chemical | 1.3 | 88.3 | [20] |
| | rGC-CNF hydrogel | chemical | 2.73 | 97.67 | [21] |
| | lignocellulose-based hydrogel | chemical | 1.84 | 86.5 | [22] |
| | carbon black/cellulose hydrogel | physicochemical | 3.68 | 97.2 | [23] |
| | cellulose/alginate/carbon black hydrogel | ionic and physical | 1.33 | 90.6 | [24] |
| | Chitosan/carboxy methyl cellulose/chitosan | physicochemical | 2.0 | 88 | [25] |
| | double-layer cellulose hydrogel | chemical | 1.58 | 91.4 | [26] |
| | hydroxypropyl cellulose | chemical | 3.11 | 91.5 | [27] |
| PVA-based hydrogels | $Ti_4O_7$-PVA | physicochemical | 4.45 | 90.69 | [28] |
| | conducting polymer/PVA | chemical | 1.83 | 82.2 | [29] |
| | oxygen-doped microporous carbon hydrogel | physicochemical | 2.44 | 95.6 | [30] |
| | PVA/Graphite | ionic and physical | 3.5 | 93 | [31] |
| | EGaIn@Ag/PVA | physicochemical | 3.26 | 95.6 | [32] |
| | g-$C_3N_4$/PVA/chitosan hydrogel | physicochemical | 3 | 98 | [33] |
| | cellulose nanofibers/PVA | chemical | 3.01 | 84.6 | [34] |
| | Nanomicelle/PVA | physicochemical | 2.19 | 96.4 | [35] |
| | $MoS_2$/sodium polyacrylate/PVA | chemical | 2.8 | 92.52 | [36] |
| | phosphotungstic acid/PVA | physicochemical | 3.88 | 94 | [37] |
| | $\lambda$-$Ti_3O_5$/PVA | chemical | 6.09 | 92.4 | [1] |
| | CS/CNT/PVA | physicochemical | 4.8 | 95 | [38] |
| | GO/CNT/$Fe_3O_4$/PVA | physical | 2.13 | 92.4 | [39] |
| PAM-based hydrogels | carbon material/PAM hydrogel | physical | 2.03 | 96.3 | [40] |
| | acetylene black/SA/PAM | physicochemical | 1.64 | 93 | [41] |
| | multi-walled C nanotubes/PAM | chemical | 2.74 | 91.6 | [42] |
| | polypyrrole/alginate/PAM | physicochemical | 4.14 | 120 | [43] |
| | PEDOT:PSS/PAM | chemical | 2.15 | 97.2 | [44] |
| SA-based hydrogels | Carbon/SA hydrogel | physical | 1.88 | 126.08 | [45] |
| | carbon dots/PVA/SA hydrogel | physicochemical | 4.79 | 92.26 | [46] |
| | MXene PVA/SA hydrogel | physicochemical | 3.6 | 87.5 | [47] |
| | BiOBr/SA hydrogel | physical | 1.99 | 78.4 | [48] |
| Other hydrogels | CMCS/$\gamma$-PGA/PDA@MWCNTs | chemical | 2.23 | 98.14 | [49] |
| | chitosan/carbon hydrogel | chemical | 4.23 | 93.1 | [50] |
| | lignin hydrogels | chemical | 2.16 | 94.2 | [51] |
| | $Fe_3O_4$ @chitosan hydrogel | physicochemical | 2.83 | 102 | [52] |

significant advantages in environmentally friendly water evaporation applications, thereby promoting the widespread use of PVA hydrogels in this field.

Yu et al. introduced an innovative method that integrates konjac glucomannan with readily synthesizable photothermal nanoparticles made from iron-based metal-organic frameworks into PVA networks. This innovative combination resulted in hybrid hydrogel evaporators capable of achieving an impressive ER of 3.2 kg $m^{-2}$ $h^{-1}$ when exposed to one sun irradiation (**Figure 5**a,b).[58] Furthermore, heavy metal ions are effectively eliminated through the formation of hydrogen bonds and chelation with the surplus -OH groups present in the hydrogel (Figure 5c). This study presents innovative opportunities for a practical and affordable solar water purification system that guarantees high water quality. Liu et al. prepared an evaporator that anchored surface-tailored liquid metal nanoparticles onto the vertically aligned microchannels of the PVA hydrogel through directional freezing, which accelerates water transportation (Figure 5d).[32] This intricate design results in an impressive ER of 3.26 kg $m^{-2}$ $h^{-1}$ under one sun illumination (Figure 5e). The hydrogel evaporator demonstrates its utility in the treatment of real seawater and dye-polluted wastewater, providing fresh perspectives on synergistic design approaches. Jiang et al. devised a novel approach for the fabrication of a self-assembling sponge-like composite hydrogel made from PVA and graphite based on the Hofmeister effect. This hydrogel demonstrates an ER of 3.5 kg $m^{-2}$ $h^{-1}$ under one sun irradiation (Figure 5f).[31] Its outstanding performance, coupled with a straightforward and

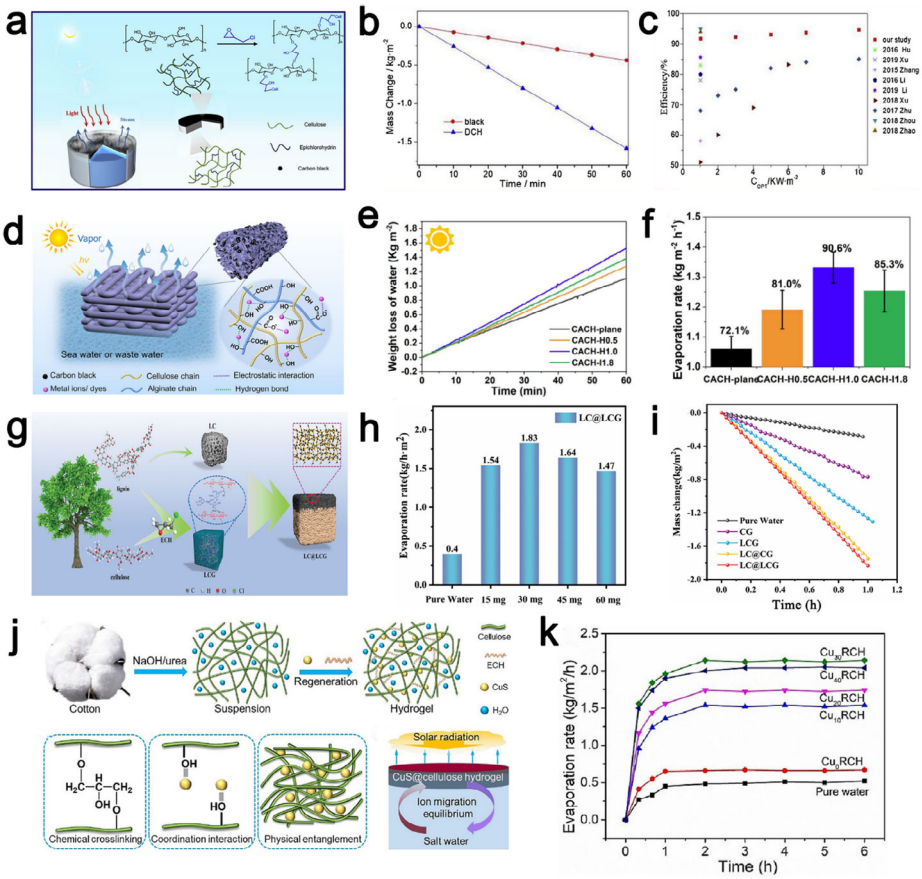


**Figure 4.** a) Preparation and solar steam generation mechanism. b) The mass change in water versus time with and without DCH under one sun. c) The solar stream efficiencies of dual-layer cellulose hydrogel. Reproduced with permission.[26] Copyright 2020, Elsevier. d) 3D-printed hydrogel. e) Weight loss of water over time under one sun irradiation. f) The ER and efficiency of hydrogel evaporators. Reproduced with permission.[24] Copyright 2022, Elsevier. g) Synthesis of lignocellulosic biomass-based double-layered porous hydrogel. h) Water ER of different hydrogel evaporators. i) Mass changes of different evaporators in pure water under one sun irradiation. Reproduced with permission.[22] Copyright 2022, Wiley-VCH. j) The process of preparing CuS@cellulose composite hydrogel. k) The ER of pure water and various hydrogels under one sun irradiation. Reproduced with permission.[54] Copyright 2023, Elsevier.

scalable preparation method, renders it an invaluable material for practical solar seawater desalination devices. Chang et al. merged photothermal $MoS_2$ hollow nanospheres and a polydopamine coating to achieve superior light absorption, combined with a PVA hydrogel matrix for PISSG.[59] Under one sun irradiation, a remarkable ER of 5.41 kg $m^{-2}$ $h^{-1}$ (pure water) was recorded, along with conversion efficiencies of 93.7%, which is attributed to the excellent water transport rate, thermal localization, and salt tolerance (Figure 5g–i). Meanwhile, it also maintains a high hydrogen production rate of 45.5 mmol $m^{-2}$ $h^{-1}$. This evaporator provides an advanced sustainable energy and water treatment solution.

PVA, as an important polymer material for synthetic hydrogels, has found extensive applications in the field of PISSG due to its excellent biocompatibility and water transport capabilities. Additionally, by modifying the surface functional groups, the hydrophilicity or hydrophobicity of the hydrogel can be altered to regulate the ER. As an environmentally friendly hydrogel material, PVA shows promising application prospects in the direction of PISSG.

### 2.3. Polyacrylamide-Based Hydrogels

PAM, a high-molecular-weight polymer derived from acrylamide monomers, exhibits high water absorption, a tunable pore structure, excellent mechanical properties, and chemical stability.[60] In the field of PISSG, the high-water absorption capacity of PAM-based hydrogels ensures a continuous water supply, while their tunable pore structure optimizes water transport and steam escape pathways, thereby enhancing evaporation efficiency. Additionally, PAM hydrogels are easily functionalized and can significantly improve light absorption and photothermal conversion efficiency by incorporating photothermal materials such as graphene and carbon nanotubes. Their chemical stability and resistance to salt render them exceptionally effective for seawater desalination and wastewater treatment, reducing the negative effects of salt crystallization on evaporation efficiency. Furthermore, the environmental friendliness, low cost, and ease of fabrication of PAM hydrogels make them an ideal material for PISSG technologies to address global water scarcity challenges.

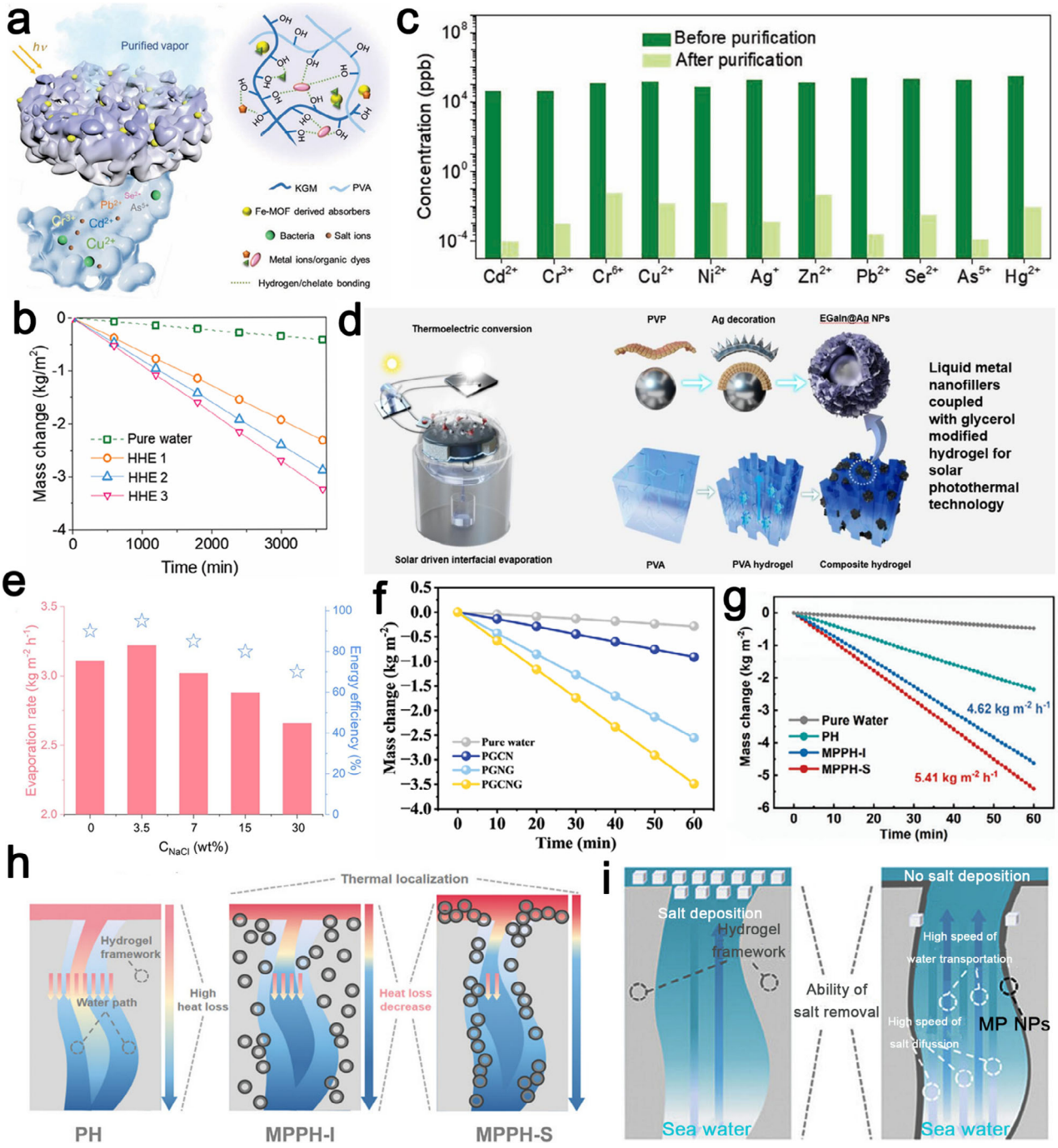


**Figure 5.** a) Solar water purification using the evaporator. b) Mass change of the prepared evaporators over time. c) The overall heavy metal removal performance of the evaporator. Reproduced with permission.[58] Copyright 2022, Wiley-VCH. d) Schematic illustration of the hydrogel evaporator. e) Water ER and energy efficiency. Reproduced with permission.[32] Copyright 2024, Elsevier. f) Mass changes under one sun irradiation for 1 h. Reproduced with permission.[31] Copyright 2024, Wiley-VCH. g) The mass changes of water over time under one sun irradiation. h) The enhancement of thermal localization by hollow nanostructure and interface assembly. i) Scheme of salt diffusion. Reproduced with permission.[59] Copyright 2024, Wiley-VCH.

Yan et al. designed a long-term stable MXene-carrageenan/PAM (MXene-CA/PAM) hydrogel evaporator that demonstrated remarkable durability by functioning continuously for 360 h without any decline in efficiency. Under one sun illumination, this innovative system maintained an impressive average ER of 1.78 kg $m^{-2}$ $h^{-1}$ (**Figure** 6a,b).[61] PAM and CA constructed a double-cross-linked, high-strength, deformation-resistant, self-healing hydrogel structure for water supply. This study introduces an innovative method for developing double-network hydrogel evaporators, improving both their

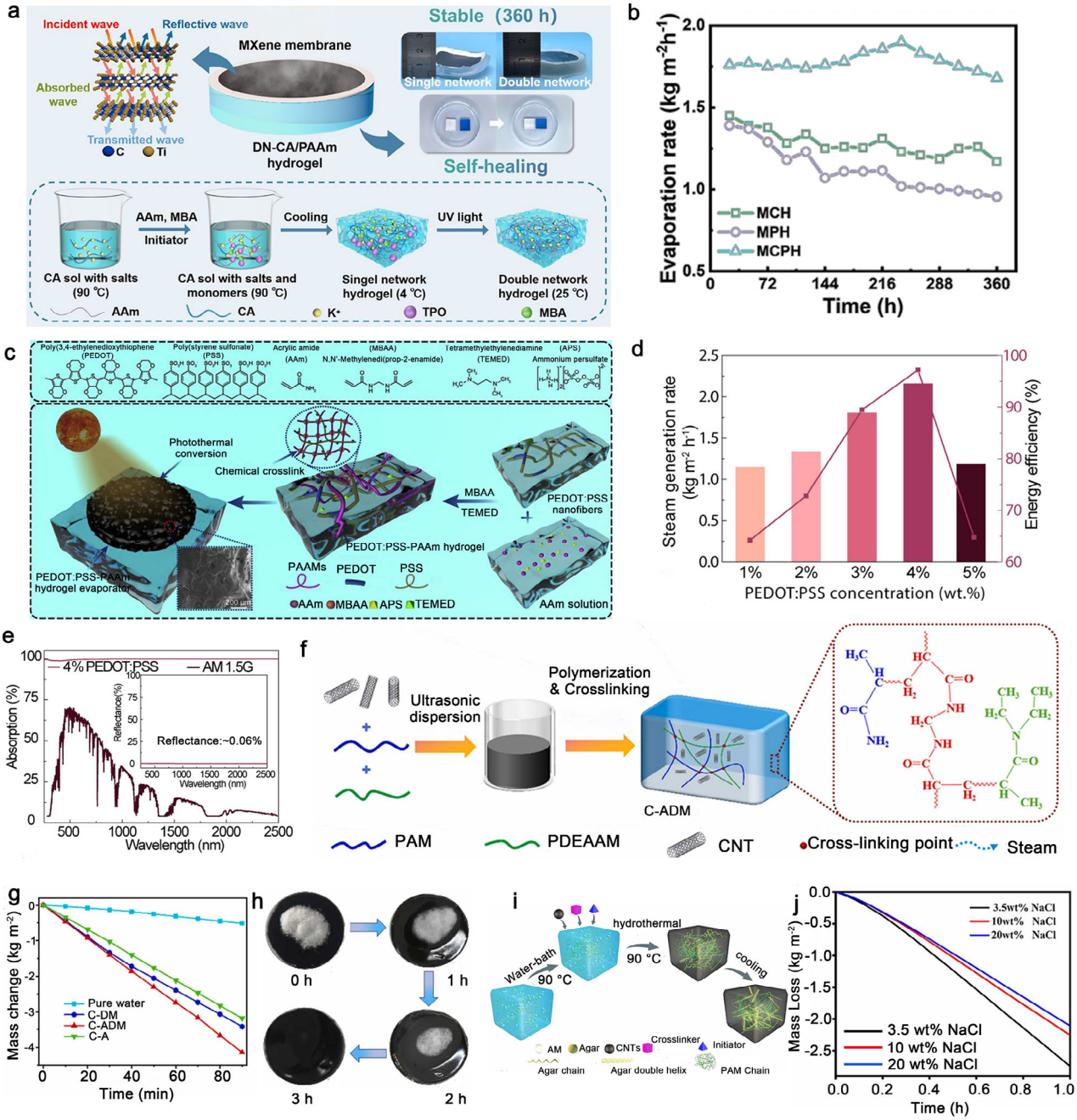


**Figure 6.** a) The preparation of the double-network hydrogel evaporator. b) ER of the prepared evaporators in simulated seawater under one sun. Reproduced with permission.[61] Copyright 2025, The Royal Society of Chemistry. c) Schematic illustration of designing dual network hydrogels. d) The absorption spectra of the hydrogels and AM 1.5G reflectance. e) The ER and energy efficiency for the prepared hydrogels. Reproduced with permission.[44] Copyright 2022, Elsevier. f) The preparation process of the light-temperature responsive hydrogel solar evaporator. g) Mass changes under dark conditions. h)The photos of the process of salt dissolving on the surface of a thermosensitive hydrogel. Reproduced with permission.[42] Copyright 2024, Elsevier. i) The fabrication process of the hydrogel evaporator. j) Evaporation test of hydrogel in varying concentrations of saline solution. Reproduced with permission.[62] Copyright 2022, Wiley-VCH.

stability and durability, and contributing to the progress of desalination technology. Lu et al. developed a dual-network hydrogel incorporating poly(3,4-ethylenedioxythiophene): polystyrene sulfonate (PEDOT:PSS) and PAM for the purpose of enhancing the efficiency of PISSG, which exhibits excellent mechanical stability under deformation and remarkable mechanical properties, highlighting its suitability for harsh practical conditions (Figure 6c).[44] The hydrogel demonstrates remarkable sunlight absorption capabilities, achieving ≈99.8%. It also exhibits a rapid ER of 2.15 kg $m^{-2}$ $h^{-1}$ and boasts an impressive energy

efficiency of ≈97.2%. (Figure 6d,e). This work further demonstrates the PAM-based hydrogel-integrated solar steam generator for practical desalination and sewage purification. Dong et al. developed an innovative composite hydrogel solar evaporator that responds to both light and temperature. This design features a hydrophilic backbone made of PAM, combined with a highly efficient solar absorbing component consisting of multi-walled carbon nanotubes, along with a temperature-sensitive polymer backbone, poly (N, N-diethylacrylamide) (Figure 6f).[42] The hydrogel demonstrates a remarkable ER of 2.74 kg $m^{-2}$ $h^{-1}$ and showcases exceptional resistance to salt (Figure 6g,h). The impressive steam generation efficiency and strong resistance to salt provide exciting possibilities for the development of ultrafast solar water purification systems. Miao et al. incorporated agar into PAM to innovatively create -OH groups on the hydrogel's framework. This modification enhances the hydrogel's durability and modulates its water content, resulting in a decreased energy requirement for evaporation and improved resistance to external perturbations (Figure 6i).[62] Consequently, an impressive ER of ≈3 kg $m^{-2}$ $h^{-1}$ is attained, along with a photothermal conversion efficiency of 86.2% under one sun illumination (Figure 6j). The -OH group-functionalized skeleton of PAM hydrogel provides an innovative strategy for constructing robust and efficient solar thermal desalination systems, demonstrating high potential for practical applications.

All in all, PAM-based hydrogels demonstrate significant advantages in PISSG due to their high water absorption capacity, tunable pore structure, excellent mechanical properties, and chemical stability. PAM-based photothermal hydrogels enable highly efficient, stable, and environmentally friendly solar-driven water evaporation, providing critical technological support for addressing global water scarcity challenges.

### 2.4. Sodium Alginate-Based Hydrogels

SA-based hydrogels, which are 3D network structures formed by crosslinking the natural polysaccharide SA with divalent cations (e.g., $Ca^{2+}$), exhibit high water absorption capacity, tunable pore structure, excellent mechanical properties, chemical stability, and environmental friendliness. The excellent water absorption capabilities of SA-based hydrogels guarantee a steady supply of water. Additionally, their adjustable pore structure improves the pathways for water transport and steam release, leading to a substantial increase in evaporation efficiency. Furthermore, SA-based hydrogels, which are characterized by excellent biocompatibility, biodegradability, and low cost, serve as an ideal material for PISSG technologies. These advantages enable SA-based hydrogels to demonstrate broad application potential in seawater desalination, providing efficient and sustainable technological solutions to address global water scarcity challenges.

Wang et al. prepared SA hydrogels combined with carbon nanotubes through their abundant hydrophilic groups (such as -OH and -COOH) to form honeycomb walls with sandwich structures (SA/carbon nanotubes (CNTs)/SA), which significantly increase the ER.[63] The hydrophilicity of SA promotes the rapid transport and storage of water, while the efficient light absorption capacity of carbon nanotubes enhances photothermal conversion efficiency (**Figure** 7a,b). This structure not only optimizes the water transport path but also rapidly transports water to the evaporation interface through capillary action. This reduces the water's evaporation enthalpy, achieving an ER of 2.25 kg $m^{-2}$ $h^{-1}$ (Figure 7c,d).

In addition, the mechanical stability and compressive properties of the SA ensure the high efficiency and durability of the evaporator during long-term use. Jiang et al. designed a porous hydrogel evaporator derived from biomass, featuring an interconnected pore architecture. Such structure was achieved through an efficient three-step process that includes foaming, freezing, and crosslinking, in which SA and PVA are utilized as the matrix materials, along with commercial graphite as the photothermal material. The hydrogel achieved an ER of 3.15 kg $m^{-2}$ $h^{-1}$ with an evaporation efficiency of 91% (Figure 7e).[64] The addition of SA not only enhances the mechanical strength and stability of the hydrogel but also provides a channel for the transport of water and the escape of steam, thereby avoiding the effects of salt crystallization on the evaporation efficiency (Figure 7f). As-developed hydrogel evaporator, which can be easily prepared, is cost-effective and biocompatible, showing significant promise for applications in solar desalination.

Moreover, Xue and coworkers created an innovative evaporator using a simple and scalable approach. This method entails the in-situ deposition of reduced graphene oxide (rGO) and SA hydrogel onto melamine sponge structures, achieved through a series of steps that include dipping, baking, and crosslinking.[65] The SA hydrogel, with its abundant hydrophilic groups that interact with rGO, significantly reduces the water evaporation enthalpy by promoting the formation of intermediate water, thereby accelerating the water evaporation process (Figure 7g). The porous structure and inherent hydrophilicity of the SA hydrogel not only optimize water transport pathways but also enable rapid water delivery to the evaporation interface via capillary action, further enhancing the ER. Furthermore, the collaborative effect of SA and rGO enhances light absorption and boosts photothermal conversion efficiency. This synergy allows the hydrogel to attain an exceptional solar-driven ER of 3.13 kg $m^{-2}$ $h^{-1}$, alongside an impressive energy conversion efficiency of 91.54%. These results underscore the hydrogel's exceptional capabilities in solar-powered water evaporation applications (Figure 7h).

Furthermore, Yuan et al. developed a vertically oriented 3D aerogel through the combination of SA and rGO, referred to as SrGAE, which demonstrated an impressive ER of 3.7 kg $m^{-2}$ $h^{-1}$ and an exceptional solar-to-steam conversion efficiency of 106% (Figure 7i).[66] The high ER is due to the structure of SA, which significantly improves water transport efficiency and salt discharge through vertically arranged microchannels. During the evaporation process, the hydrogel utilizes capillary forces to continuously supply water and absorbs external energy through evaporative cooling. This process reduces the water evaporation enthalpy and effectively improves photothermal conversion efficiency (Figure 7j). Combined with low thermal conductivity and excellent salt repulsion, these properties enable the hydrogel to exhibit outstanding performance in brine evaporation, resulting in an efficient ER.

SA-based hydrogels enable highly efficient, stable, and environmentally friendly solar-driven water evaporation, providing critical technological support for addressing global water scarcity challenges.

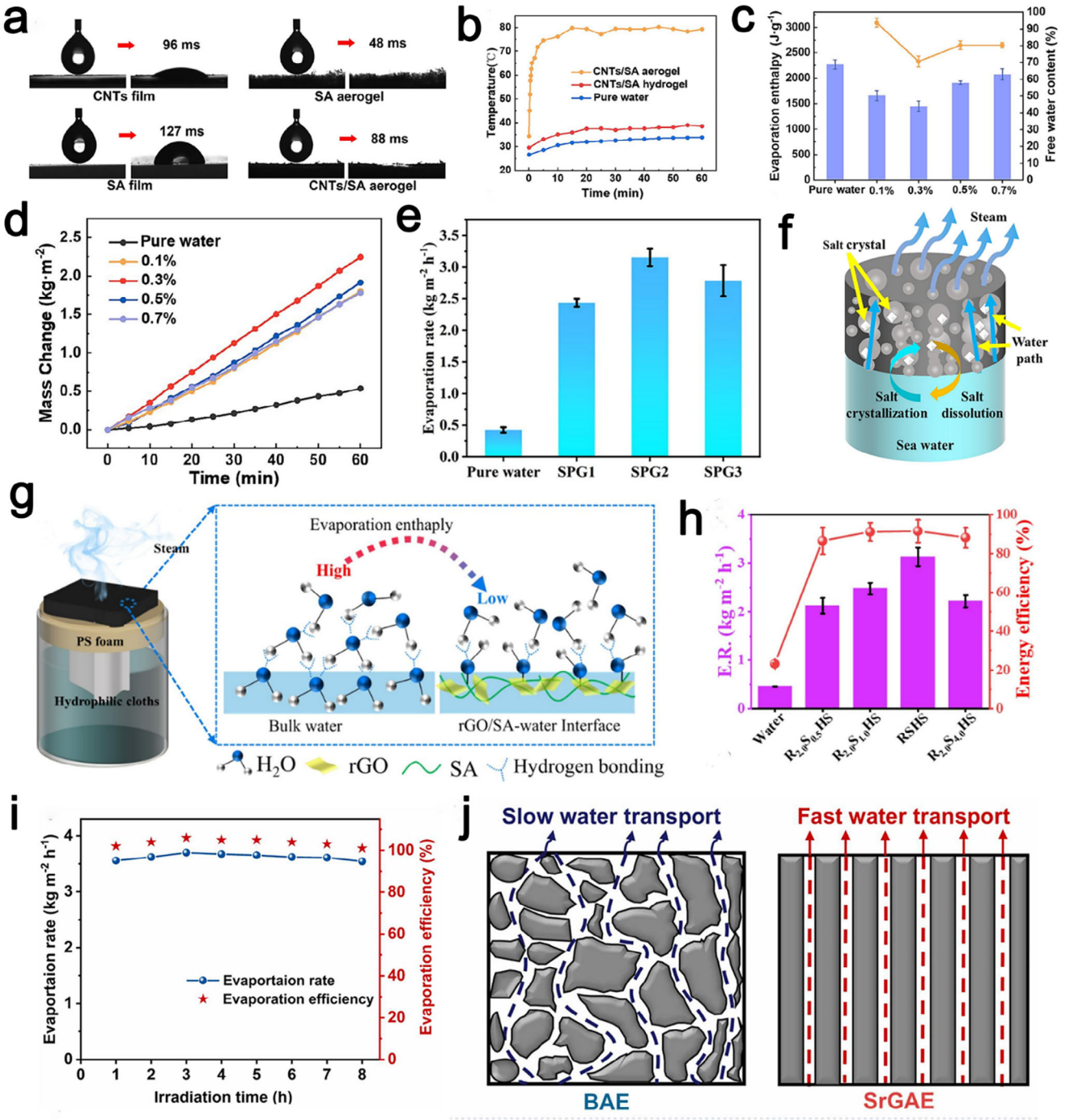


**Figure 7.** a) Water wetting behavior of the prepared samples. b) Temperature variation of different sample surfaces with time at one sun irradiation. c) Enthalpy of water evaporation and free water content within the SA/CNTs/SA hydrogel. d) Water vapor generation rate of different samples. Reproduced with permission.[63] Copyright 2025, Elsevier. e) The ER and f) schematic of the salt resistance of the evaporator during the solar evaporation process. Reproduced with permission.[64] Copyright 2024, Elsevier. g) Schematic diagram of the evaporation system. h) ER of water and the corresponding energy efficiencies. Reproduced with permission.[65] Copyright 2023, Elsevier. i) The ER and efficiency of SrGAE. j) Schematic description of the water transport. Reproduced with permission.[66] Copyright 2025, Elsevier.

### 2.5. Other Substrates-Based Hydrogels

In addition to the above hydrogels, a variety of hydrogel evaporators utilizing different substrates have also been developed.[67] Zhang and colleagues prepared a composite hydrogel utilizing carboxymethyl chitosan (CMCS), poly($\gamma$-glutamic acid) ($\gamma$-PGA), and polydopamine-modified multi-walled CNTs (PDA@MWCNTs) through a one-pot synthesis method for PISSG.[49] CMCS, a chitosan derivative, is characterized by its rich hydrophilic groups within its macromolecular structure. Meanwhile, the water solubility, exceptional absorbency, and biodegradability of $\gamma$-PGA contributed to an impressive ER of 2.23 kg $m^{-2}$ $h^{-1}$. Li et al. introduced a novel approach that combines freeze-casting with alkali infiltration to successfully construct hierarchical porous chitosan/carbon black sponge-like hydrogels. This innovative strategy results in evaporators that exhibit remarkable resistance to deformation, rapid water transport, and improved salt circulation, ultimately achieving an outstanding ER of 4.23 kg $m^{-2}$ $h^{-1}$ and high-salinity desalination.[50]

In addition, hydrogels derived from lignin are regarded as exceptionally promising candidates for PISSG, owing to the renewable and biocompatibility characteristics of lignin. Qi et al. prepared a lignin hydrogel that shows an excellent ER of 2.16 kg $m^{-2}$ $h^{-1}$ and an efficiency of 94.2%.[51] Wang et al. prepared a 3D chitosan-based hydrogel evaporator with a directional vertical channel structure, which achieved stable performance even in saturated brine (salinity of 26.47 wt.%), with an excellent ER of 2.83 kg $m^{-2}$ $h^{-1}$ and no salt crystal accumulation after continuous evaporation for over 8 h.[52] In a word, hydrogels with different substrates provide new perspectives and possibilities for the development of PISSG technology.

## 3. Properties and Photothermal Conversion Mechanisms of Hydrogels

### 3.1. Physicochemical Properties of Hydrogels Affecting PISSG Performance

The performance of hydrogels in PISSG is significantly influenced by their key physicochemical properties, which can be divided into the following three aspects, such as microstructure, macroscopic appearance, and the regulation of evaporation enthalpy. The microstructure includes the pore structure, which governs water transport and evaporation efficiency; water evaporation pathways, which are critical for water delivery and evaporation, minimizing thermal loss; and hydrophilicity, which determines water absorption and retention capabilities. The macroscopic appearance includes mechanical strength, which ensures structural stability under operational conditions; surface roughness, which affects light absorption and photothermal conversion efficiency, and bionic structure which significantly affects energy efficiency. The regulation of evaporation enthalpy, which can be achieved by modifying the surface functional groups to alter the hydrophilicity of the evaporator, not only affects the water absorption and retention capabilities of the evaporator but also influences its evaporation enthalpy by adjusting the ratio of intermediate water to free water; Constructing porous materials allows for the adsorption of more water to form water clusters, which break surface hydrogen bonds with less energy required. Additionally, the Hofmeister effect lowers the energy barrier for water molecules escaping, consequently reducing the thermodynamic enthalpy required for evaporation. Together, these properties synergistically determine the overall efficiency and applicability of hydrogels in PISSG systems.

#### *3.1.1. The Microstructure of Hydrogels*

1) **Pore Structure:** The pore structure of hydrogels significantly influences their performance in PISSG, which is primarily reflected in several aspects. First, the pore structure determines the efficiency of water transport, with larger pores and well-connected channels accelerating water diffusion and ensuring a constant water supply to the evaporation surface.[52,68] Second, the porous structure provides a larger evaporation area, which allows water to be more readily exposed to the evaporation interface, thereby enhancing the ER. Additionally, the pore structure affects the distribution of photothermal materials and light absorption capacity, optimizing photothermal conversion efficiency and improving thermal management, which prevents localized overheating and heat loss. Moreover, a rationally designed pore structure enhances the mechanical stability of hydrogels, preventing them from collapsing or deforming during the evaporation process. Finally, in applications such as seawater desalination, larger pores help reduce salt deposition, improving salt resistance and extending the service life.

Yu et al. fabricated large-scale elastic hydrogel evaporators using a self-assembled template method.[69] The research indicates that the hydrogel's highly interconnected porous structure, characterized by low tortuosity and adjustable pore dimensions, allows for accurate control over the rates of water transport. The pore sizes of hydrogels vary from 5, 75, 170, to 390 μm, and the water transport rates range from 0.62 to 621.9 g $min^{-1}$, which indicates a strong dependency on pore size (**Figure** 8a,b). Experimental results demonstrate that this optimal porous hydrogel exhibits high evaporation performance under natural light, achieving an ER of 2.8 kg $m^{-2}$ $h^{-1}$ and a solar-to-steam conversion efficiency of ≈90% (Figure 8c,d). Therefore, by controlling the pore size and porosity structure of the hydrogel, the water transport and evaporation performance can be effectively optimized. This provides new insights for the large-scale production of efficient and durable solar evaporators, advancing their practical applications in clean water production. A hydrogel thin film with interconnected microporous channels is proposed by Ma and colleagues.[70] This microporous structure not only significantly reduces heat loss (by 88%) but also improves energy efficiency to 98% by optimizing the heat transfer cross-sectional area (Figure 8e,f). Simultaneously, the interconnected pores facilitated rapid water transport to the evaporation interface, preventing localized drying and maintaining a high, sustained ER of 4.14 kg $m^{-2}$ $h^{-1}$ (Figure 8g,h).

Therefore, optimizing the pore structure of hydrogels, which is a critical strategy for enhancing their photothermal evaporation efficiency, plays a pivotal role in advancing PISSG performance.

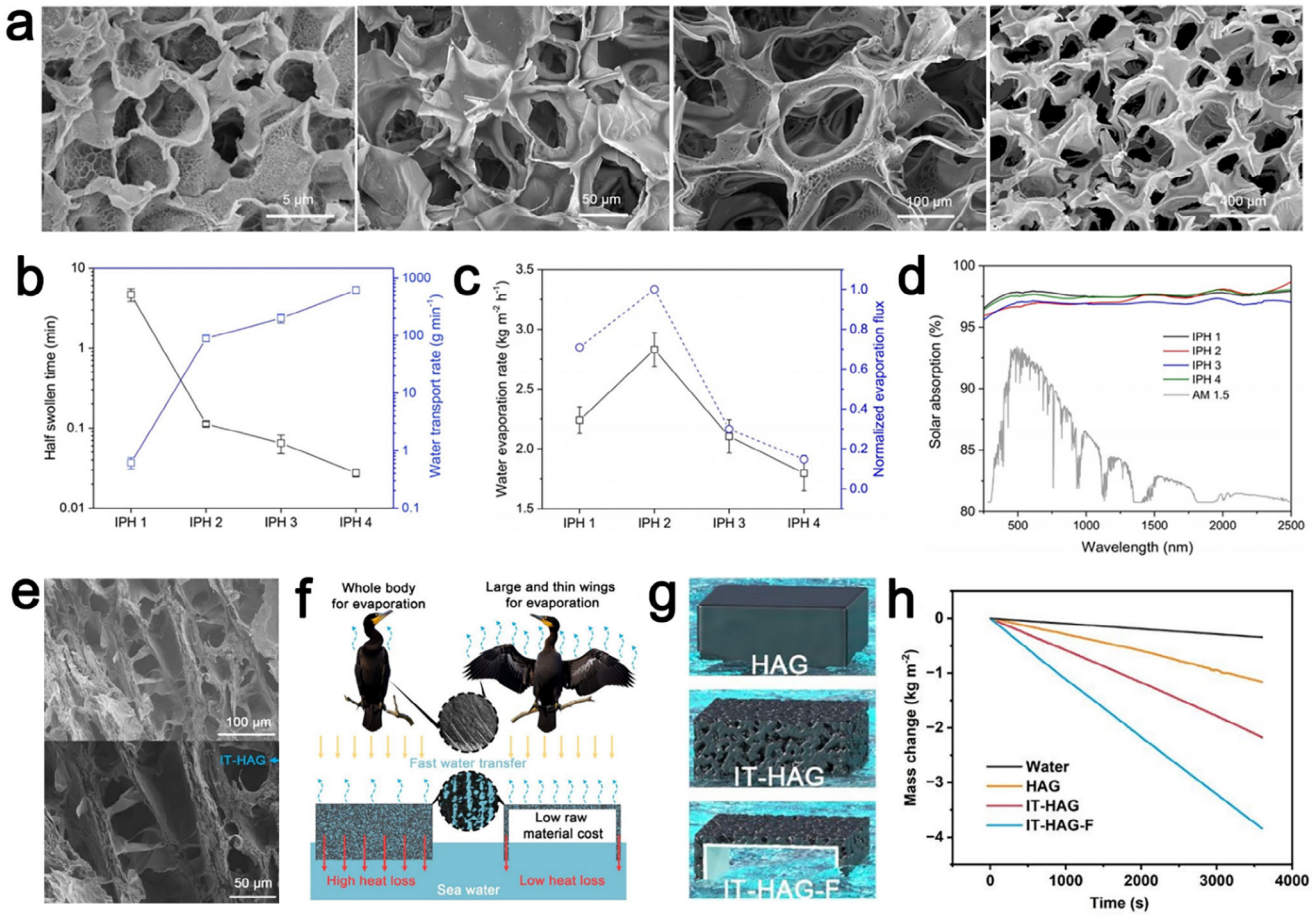


**Figure 8.** a) SEM images of evaporators with different pore sizes: 5, 75, 170, and 390 μm. b) Swelling behavior and the calculated water transport rate of evaporators. c) The water ER, and d) UV–vis–NIR spectra of evaporators. Reproduced with permission.[69] Copyright 2022, Wiley-VCH. e) The SEM images of ice template hydrophobic association gel. f) Schematic of cormorant-inspired macro-porous hydrogel thin film. g) Schematic diagram of hydrophobic association gel, hydrophobic association gel, and ice template hydrophobic association gel film structure. h) The mass loss of water based on different evaporators under one sun irradiation. Reproduced with permission.[70] Copyright 2023, The Royal Society of Chemistry.

2) **Water evaporation pathway:** The water evaporation pathway within hydrogels significantly influences their performance in PISSG, as evidenced by several key aspects. First, an optimized water evaporation pathway reduces water transport resistance, enabling rapid and uniform water delivery to the evaporation interface, thereby enhancing the ER.[71] Second, a well-designed pathway can localize heat at the evaporation interface, minimizing heat loss to the bottom or surrounding environment of the hydrogel and improving thermal utilization efficiency.[45] Additionally, an efficient water evaporation pathway ensures a continuous and sufficient water supply to the evaporation interface, preventing performance degradation due to water scarcity or drying. In applications such as seawater desalination, an optimized pathway can mitigate salt accumulation at the evaporation interface, delaying salt crystallization and maintaining stable evaporation performance while extending the operational lifespan. Moreover, the design of the water evaporation pathway affects heat distribution, and a rational pathway facilitates uniform heat transfer to the evaporation interface, avoiding localized overheating or heat concentration. Lastly, by regulating the water evaporation pathway, diverse hydrogel structures, such as vertical channels or gradient porosity, can be achieved to meet the requirements of various application scenarios. Therefore, optimizing the water evaporation pathway is a critical strategy for improving the photothermal evaporation efficiency of hydrogels.

Li et al. developed anisotropic PVA/MXene composite hydrogels designed for effective solar-driven water evaporation, employing a template-assisted directional freezing method.[72] Such directional channel architecture not only reduces water transport resistance but also synergizes with the PVA framework to lower the evaporation enthalpy of water, further boosting the ER up to2.55 kg $m^{-2}$ $h^{-1}$ (**Figure 9**a,b). Additionally, the integration of directional channels with MXene sheets enhances the structural stability of the hydrogel and optimizes solar-thermal conversion efficiency (Figure 9c,d). By designing a hydrogel evaporator with a multi-level radial structure (PCC-RD), Chen et al. successfully achieved an efficient balance between water transport and thermal management.[34] The central axial channel of the PCC-RD hydrogel ensures rapid vertical water transport, while the surrounding radial channels provide multi-directional

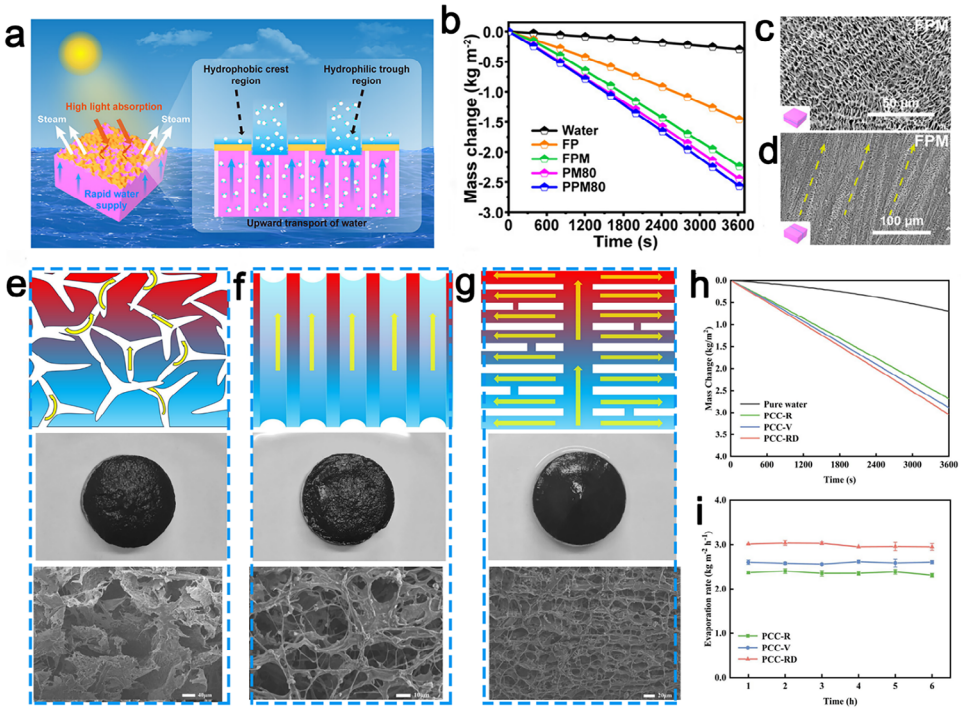


**Figure 9.** a) Hydrogel evaporator for efficient solar-driven steam generation. b) The mass changes of different evaporators under one sun irradiation. The SEM images of c) the internal cross-section and d) the vertical section of the hydrogel evaporator. Reproduced with permission.[72] Copyright 2024, The American Chemical Society. Schematic structure of water transport, photographs, and SEM images in e) PCC-R, f) PCC-V and g) PCC-RD. h) Mass changes of water in different hydrogel evaporators. i) The ER of the prepared three hydrogel evaporators in 20 wt.% NaCl. Reproduced with permission.[34] Copyright 2025, Elsevier.

water transport pathways, ensuring that water can be rapidly and uniformly delivered to the evaporation interface. Such structural design enables the PCC-RD hydrogel to achieve a high ER of 3.01 kg $m^{-2}$ $h^{-1}$ under one sun illumination, which is significantly higher than that of the random structure (PCC-R) and vertical structure (PCC-V) hydrogels (Figure 9e–i). Additionally, the radial channels act as thermal barriers, reducing downward heat conduction losses and further enhancing evaporation efficiency. The low evaporation enthalpy (1091.06 J $g^{-1}$) of the PCC-RD hydrogel indicates that it can achieve faster ER with lower energy requirements. Therefore, the water transport channels in the hydrogel significantly improve the ER and efficiency by optimizing water supply and thermal localization, providing new design insights for PISSG technologies.

3) **Hydrophilicity:** The hydrophilicity of hydrogels, which play a critical role in PISSG, significantly affects their performance through multiple mechanisms. First, highly hydrophilic hydrogels exhibit exceptional water absorption capacity, ensuring a continuous water supply for sustained evaporation. Second, their superior water retention capability minimizes water loss and extends the evaporation duration. Additionally, hydrophilicity enhances the efficiency of water transport by facilitating rapid diffusion and uniform distribution within the porous structure, which optimizes the evaporation process. Moreover, the hydrophilic nature enables the formation of a uniform water film at the evaporation interface, increasing the evaporation area and reducing heat loss. Finally, the synergy between hydrophilicity and photothermal conversion efficiency, which combines absorbed water with heat generated by photothermal materials, significantly enhances evaporation performance.

As demonstrated by Zhang et al., the hydrophilicity and hydrophobicity of the hydrogel can be modulated by embedding hydrophilic 2D materials (rGO and MXene) into the hydrogel skeleton.[30] The hydrophilic surfaces and channels facilitate rapid water transport and distribution through hydrogen bonding interactions, ensuring efficient water delivery to the evaporation interface (**Figure 10**a,b). Additionally, the introduction of hydrophilic materials enhances the water absorption capacity of the hydrogel, further improving evaporation efficiency. Therefore, optimizing the hydrophilicity and hydrophobicity of hydrogels, which improves water transport and reduces evaporation enthalpy, significantly increases the ER (2.44 kg $m^{-2}$ $h^{-1}$) and efficiency (Figure 10c). Thomas and coworkers created a dual-region hydrogel that combines a covalent organic framework (COF) with graphene.[73] This innovative material features both hydrophilic and hydrophobic regions, achieved through a facile in-situ growth strategy. The dual-region hydrogel (CGH), in which hydrophilic COF covers parts of the hydrophobic rGO regions, enables precise control over the ratio of hydrophilic to hydrophobic areas, leading to enhanced light absorption, tunable wettability, optimized water content, and reduced evaporation enthalpy (Figure 10d). The hydrophilic COF regions, which

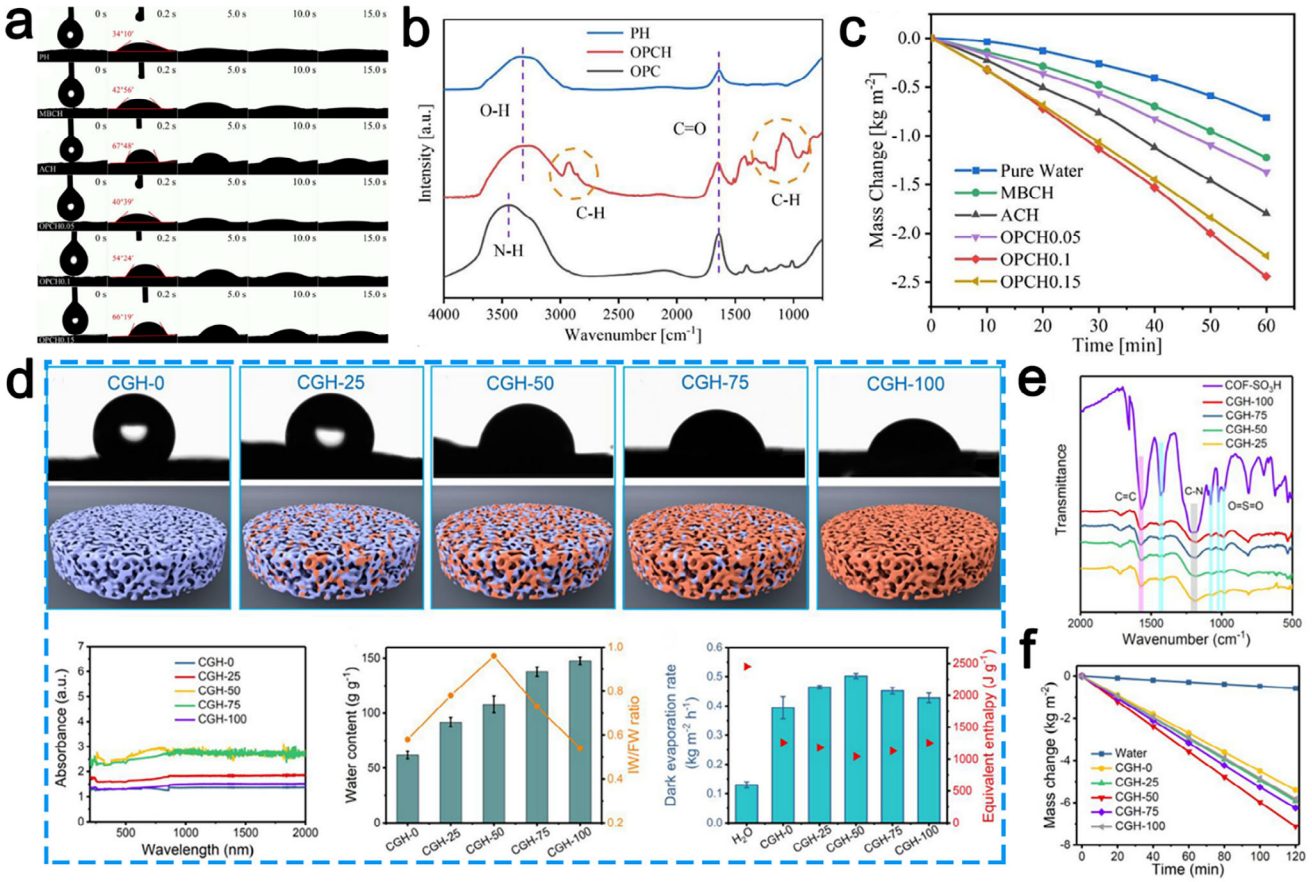


**Figure 10.** a) Dynamic contact angle and b) the FTIR spectra in the different evaporators. c) The mass change of water during water evaporation under one sun. Reproduced with permission.[30] Copyright 2024, Elsevier. d) Water contact angles, UV–vis–NIR absorbance, water content, and the ratio of intermediate water, dark ER, and evaporation enthalpy of samples prepared. e) FT-IR spectra of COF-$SO_3H$ and CGHs. f) The mass change of prepared evaporators under one sun irradiation. Reproduced with permission.[73] Copyright 2022, The American Chemical Society.

provide abundant sulfonic acid groups, promote rapid water transport and distribution through electrostatic interactions and hydrogen bonding with water molecules, while simultaneously lowering the energy required for evaporation (Figure 10e). The hydrophobic rGO regions, on the other hand, contribute to the structural stability and light absorption capacity of the hydrogel. By optimizing the ratio of hydrophilic to hydrophobic regions, the CGH achieves a high ER of 3.69 kg $m^{-2}$ $h^{-1}$ under one sun illumination, significantly outperforming pure rGO hydrogels (Figure 10f). Furthermore, the introduction of hydrophilic regions increases the proportion of intermediate water, which exhibits weaker interactions with surrounding water molecules and thus evaporates more rapidly.

In a word, optimizing the hydrophilicity of hydrogels, which is a key factor in enhancing photothermal evaporation performance, is essential for advancing PISSG systems.

In summary, the intrinsic relationship between the pore structure of hydrogels and their water transport pathways is primarily dependent on the synergistic effects of pore size, connectivity, and interfacial properties. Specifically, the size of the pores, directly regulates the water transport mechanism, allowing rapid water movement through micron-sized macropores, whereas nanopores significantly reduce permeability due to increased diffusion resistance.[74] Furthermore, the connectivity of the pore network determines the effectiveness of transport pathways. Highly connected porous structures create continuous water channels, while isolated pores or highly tortuous paths extend diffusion distances and diminish transport efficiency. Additionally, the chemical characteristics of hydrogels, such as hydrophilicity or hydrophobicity, influence water transport through interfacial interactions. Hydrophilic groups facilitate interfacial water transport, whereas hydrophobic regions may induce capillary resistance. Moreover, hydrophilic groups can dynamically modulate pore size through swelling. Therefore, the design of hydrogel pore structures fundamentally represents a critical scientific challenge in optimizing water transport functionality.

### *3.1.2. The Macroscopic Features of Hydrogels*

1) **Mechanical strength:** The mechanical strength of hydrogels influences the PISSG performance through various mechanisms. First, high mechanical strength ensures structural integrity during evaporation, preventing collapse or deformation caused by water loss or external pressure, thereby maintaining efficient water transport pathways and ER.

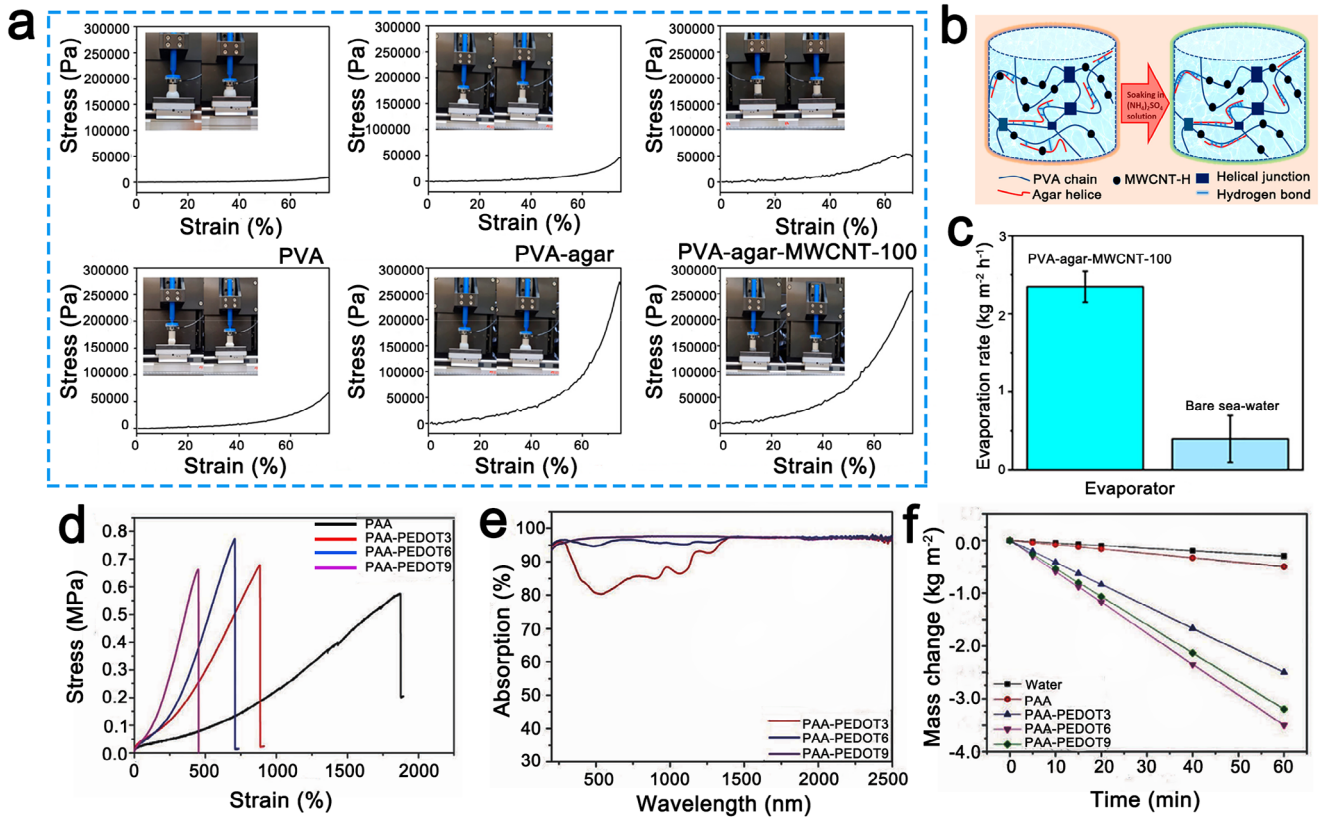


**Figure 11.** a) Compressive stress-strain curves of prepared evaporators. b) The mechanism of increased hydrogen bonds. c) The ER of the PVA-agar–carbon nanotubes hydrogel for seawater. Reproduced with permission.[75] Copyright 2022, The American Chemical Society. d) Stress-strain curves of hydrogels synthesized with varying durations of PEDOT polymerization. e) UV–vis–NIR absorption spectra of hydrogels. f) Mass changes of pure water and oriented PAA-PEDOT hydrogels under one sun illumination. Reproduced with permission.[76] Copyright 2021, Wiley-VCH.

Second, it enhances the durability of hydrogels, enabling them to resist fatigue and wear over extended periods, ensuring long-term performance stability. Additionally, mechanical strength directly affects the degree of deformation during evaporation, preventing structural shrinkage or distortion that could hinder water transport. Moreover, hydrogels with high mechanical strength exhibit improved resistance to environmental disturbances, such as mechanical impacts or water flow, ensuring functionality under harsh conditions. Finally, robust mechanical properties enable the integration of multifunctional features, such as embedding photothermal materials or designing complex pore structures, without compromising structural integrity.

Lee and coworkers proposed a 3D PVA-based hydrogel resulting in remarkable mechanical strength and making it highly effective for solar desalination applications.[75] The results of the mechanical strength tests on hydrogels indicate that single-network PVA exhibits inadequate mechanical strength. After the incorporation of agar as a double-network polymer hydrogel, the mechanical strength of PVA hydrogels experienced a significant enhancement, increasing from 0.9 to 45 kPa. Furthermore, the addition of multi-walled carbon nanotubes was observed to slightly increase the compressive strength to 52 kPa (**Figure 11a**). The remarkable increase in mechanical strength can be ascribed to the improved intermolecular hydrogen bond, higher cross-linking density, and the specific ratios of PVA and agar within the dual polymer network, as demonstrated in Figure 11b. As-developed evaporator achieved a noticeable ER of 3.1 kg $m^{-2}$ $h^{-1}$ under one sun irradiation, which paves the way for fabricating mechanically strong hydrogel evaporators for effective and sustainable solar desalination (Figure 11c). In addition, Ran et al. prepared a PAA-PEDOT hydrogel featuring a unique core-shell structure that combines high mechanical strength (tensile strength ≈780 kPa) and excellent photothermal properties (photothermal conversion efficiency ≈ 95%) (Figure 11d,e).[76] The high mechanical strength ensures that the hydrogel maintains a stable porous structure during the process of PISSG, effectively facilitating water transport and evaporation. The structural stability not only enhances the durability of the hydrogel but also enables it to achieve a high-water ER of up to 3.05 kg $m^{-2}$ $h^{-1}$ under one sun irradiation (Figure 11f). Therefore, the high mechanical strength of the hydrogel, which supports structural integrity and optimizes photothermal conversion efficiency, directly contributes to its efficient water evaporation performance, making it highly suitable for applications in PISSG.

All in all, in practical applications such as seawater desalination or wastewater treatment, high mechanical strength allows hydrogels to withstand complex environmental conditions,

ensuring consistent evaporation performance. Meanwhile, optimizing the mechanical strength of hydrogels, which is essential for enhancing their photothermal evaporation efficiency and practicality, plays a pivotal role in advancing PISSG systems.

2) **Surface roughness:** The surface roughness of hydrogel significantly influences the performance of PISSG through several key mechanisms: First, high surface roughness enhances light absorption by increasing the interaction path of incident light through multiple reflections and scattering, thereby improving photothermal conversion efficiency.[77] Second, a rough surface expands the effective evaporation area of hydrogels, exposing more water to the evaporation interface and accelerating the evaporation process. Additionally, appropriate surface roughness optimizes the wettability of hydrogels, promoting uniform water film formation and improving evaporation efficiency while reducing heat loss. Moreover, the increased surface area and improved heat distribution associated with rough surfaces enhance thermal management, preventing localized overheating and maximizing heat utilization. Finally, surface roughness facilitates the rapid escape of steam at the evaporation interface, minimizing steam retention and further boosting the ER. Beyond this, rough surfaces reduce light reflection losses, increase light energy utilization, and enhance photothermal conversion efficiency. Therefore, optimizing the surface roughness of hydrogels, which is essential for enhancing photothermal evaporation efficiency, represents a critical strategy for advancing PISSG systems.[27]

The surface roughness of the hydrogel is achieved through the design of concave pyramid-shaped surface patterns developed by Yang's team.[78] The rough surface structure not only enhances multiple reflections and absorption of light but also accelerates water flow near the evaporation interface by inducing the Marangoni effect (**Figure 12**a–c). This surface design enables the hydrogel to achieve a high ER of 3.62 kg $m^{-2}$ $h^{-1}$ under one sun illumination, significantly higher than that of smooth-surfaced hydrogels (Figure 12d,e). Additionally, the rough surface structure reduces heat conduction losses, further improving evaporation efficiency. Therefore, optimizing the surface roughness of the hydrogel, which enhances light absorption and accelerates water flow, significantly increases the ER and efficiency. Yu et al. fabricated PVA hydrogels with distinct surface morphologies, including flat surfaces (F-SH), grooved surfaces (G-SH), and sharply dimpled surfaces (D-SH), using a template-assisted gelation method (Figure 12f).[79] D-SH features a sharply dimpled surface structure that provides a larger surface area and higher roughness, enabling it to concentrate heat more effectively and reduce energy loss, thereby generating a higher heat flux per unit area. This optimized surface morphology enables D-SH to achieve an ER of ≈2.6 kg $m^{-2}$ $h^{-1}$ under one sun irradiation, with an energy efficiency of up to 91% (Figure 12g). In contrast, F-SH with a flat surface and G-SH with a grooved surface, both having smaller surface areas and weaker heat concentration effects, exhibited lower ER and energy efficiencies (Figure 12h). Therefore, the increased surface roughness of the hydrogel, which enhanced heat flux and minimized energy loss, significantly improved the ER, offering new insights for the design of efficient solar evaporators.

3) **Bionic structure:** Bionic structures, inspired by the highly efficient mechanisms found in natural organisms related to mass transfer, heat transfer, and interfacial properties, are beneficial to significantly enhancing the performance of hydrogel evaporators.[80] Specifically, the bionic structures-based design achieves efficient water transport by mimicking the hierarchical porous networks of plant xylem or animal blood vessels, reducing water flow resistance and thereby facilitating rapid water movement.[81] In terms of interfacial evaporation, the micro- and nanoscale structures observed on lotus leaves, as well as the hydrophilic-hydrophobic gradients present on insect wings, are utilized to effectively regulate the characteristics of the evaporation interface, thereby improving evaporation efficiency.[82] Furthermore, by emulating biological thermal regulation strategies, thermal management during evaporation is optimized, balancing the heat required for evaporation with environmental heat loss.

Wang et al. developed a biomimetic evaporator utilizing an innovative composite material composed of $TiO_2$, $Ti_3C_2$, $C_3N_4$, and PVA.[83] Inspired by the natural processes of plants, photocatalysis, as a photo-driven interfacial process, can be effectively integrated with solar-driven interfacial evaporation to generate clean steam (1.54 kg $m^{-2}$ $h^{-1}$) while simultaneously removing volatile organic compounds (VOCs) (**Figure 13**a). Drawing inspiration from the tree transpiration and the intricate hierarchical porous structures, Zhang et al. designed a 3D-printed bionic hydrogel evaporator (3DP-BHE) aimed at facilitating long-term solar desalination (Figure 13b).[84] This bio-inspired leaf structure with exceptional light absorption (94.01%) possesses effective steam diffusion capabilities. The 3DP-BHE achieved a stable ER of 2.13 kg $m^{-2}$ $h^{-1}$ and an energy efficiency (90.5%). Such excellent performance is attributed to the bioinspired trunk layer with porous architecture, which facilitates water transport, thermal insulation, and the convection and diffusion of salt ions.

In addition, Chen et al. prepared a PVA-based hydrogel evaporator inspired by sunflowers (Figure 13c).[85] It achieved an ER of 3.0 kg $m^{-2}$ $h^{-1}$ and an energy efficiency of 97.2%, which is attributed to the vertical structure promoting rapid water transfer and multiple reflections enhancing solar absorption efficiency. Yu et al. also demonstrated a low-cost and robust sunflower-pith-based hydrogel-like evaporator using a simple dip-coating and soaking process (Figure 13d).[86] The rigid cellular framework and the water encapsulated inside endow this evaporator with excellent compressive strength, allowing for long-time use of the evaporator. Meanwhile, the evaporator achieved an outstanding water ER of 3.39 kg $m^{-2}$ $h^{-1}$ with an energy efficiency of 100.2%.

Moreover, Sun et al. developed a biomimetic light-trapping structure, drawing inspiration from the unique surface of moth eyes, to be utilized in a multilayer interfacial evaporator aimed at improving light absorption (Figure 13e).[87] This innovative design, which mimics the light-trapping features found in both eyes, demonstrates an almost negligible reflection of sunlight, contributing to an impressive light absorption efficiency of 96.7% and a remarkable ER of 2.78 kg $m^{-2}$ $h^{-1}$ when exposed to a

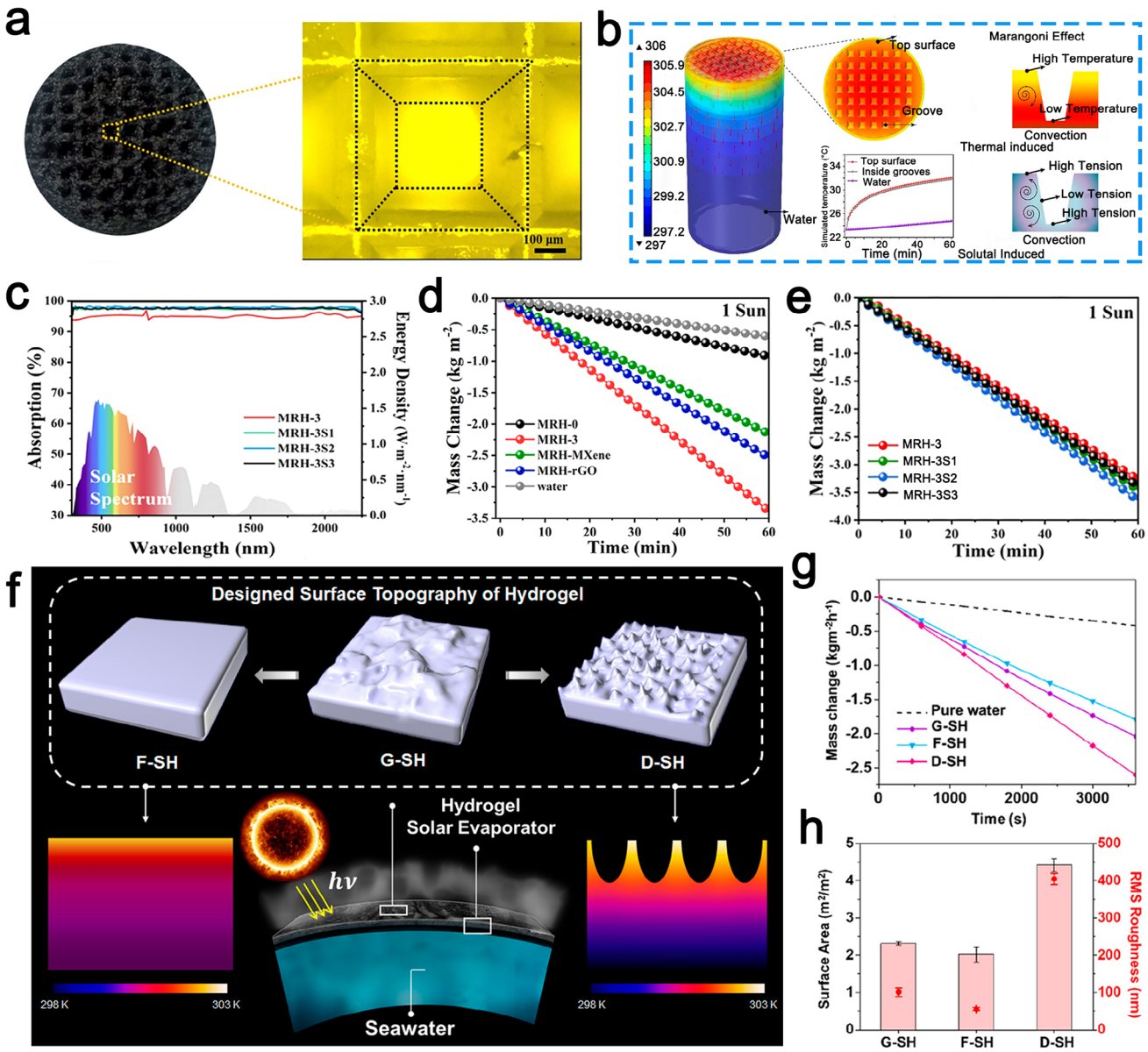


**Figure 12.** a) Schematic illustration of the surface-textured hydrogel evaporator for solar evaporation. b) Numerical simulation of evaporators. c) UV–Vis–NIR absorption spectra and corresponding energy efficiency of the textured hydrogel evaporator. Weight loss of (d) the flat hydrogel evaporator and e) the surface-textured hydrogel evaporator. Reproduced with permission.[78] Copyright 2021, The American Chemical Society. f) Schematic of surface-textured hydrogel for enhanced water ER. g) The mass change of water under one sun irradiation. h) The surface area and root-mean-square roughness of each evaporator. Reproduced with permission.[79] Copyright 2019, The American Chemical Society.

light intensity equivalent of one sun. Zhang et al. developed a biomimetic hydrogel evaporator inspired by the transpiration process of mushrooms (Figure 13f).[88] The distinctive structural configuration effectively reduces heat conduction to the water, minimizes the surface area of the water transport layer, and features a gradient architecture that helps lower thermal dissipation. This design creates a thermal barrier within the water transport layer, effectively localizing heat to the evaporation layer. Consequently, the evaporator demonstrates outstanding performance, attaining a pure water ER of 3.78 kg $m^{-2}$ $h^{-1}$ and an energy efficiency of 98.07%. A biomimetic 3D hydrogel evaporator, inspired by the gill filaments of rhubarb fish and hogweed, has been prepared, incorporating a bidirectional liquid delivery system (Figure 13g).[89] The gill filament structure facilitates longitudinal ion recirculation, while the microcavity groove patterns arranged in a mimic lip margin configuration promote lateral ion convection, thereby enabling multidirectional cross-flow migration of salt ions. This design significantly enhances the evaporation performance of pure water, achieving an ER of 2.53 kg $m^{-2}$ $h^{-1}$ and an energy efficiency as high as 99.3%.

Bionic structures, which emulate the efficient mass-heat transfer mechanisms inherent in natural biological systems, significantly enhance the PISSG performance of hydrogel-based evaporators through multifaceted optimizations: The multiscale

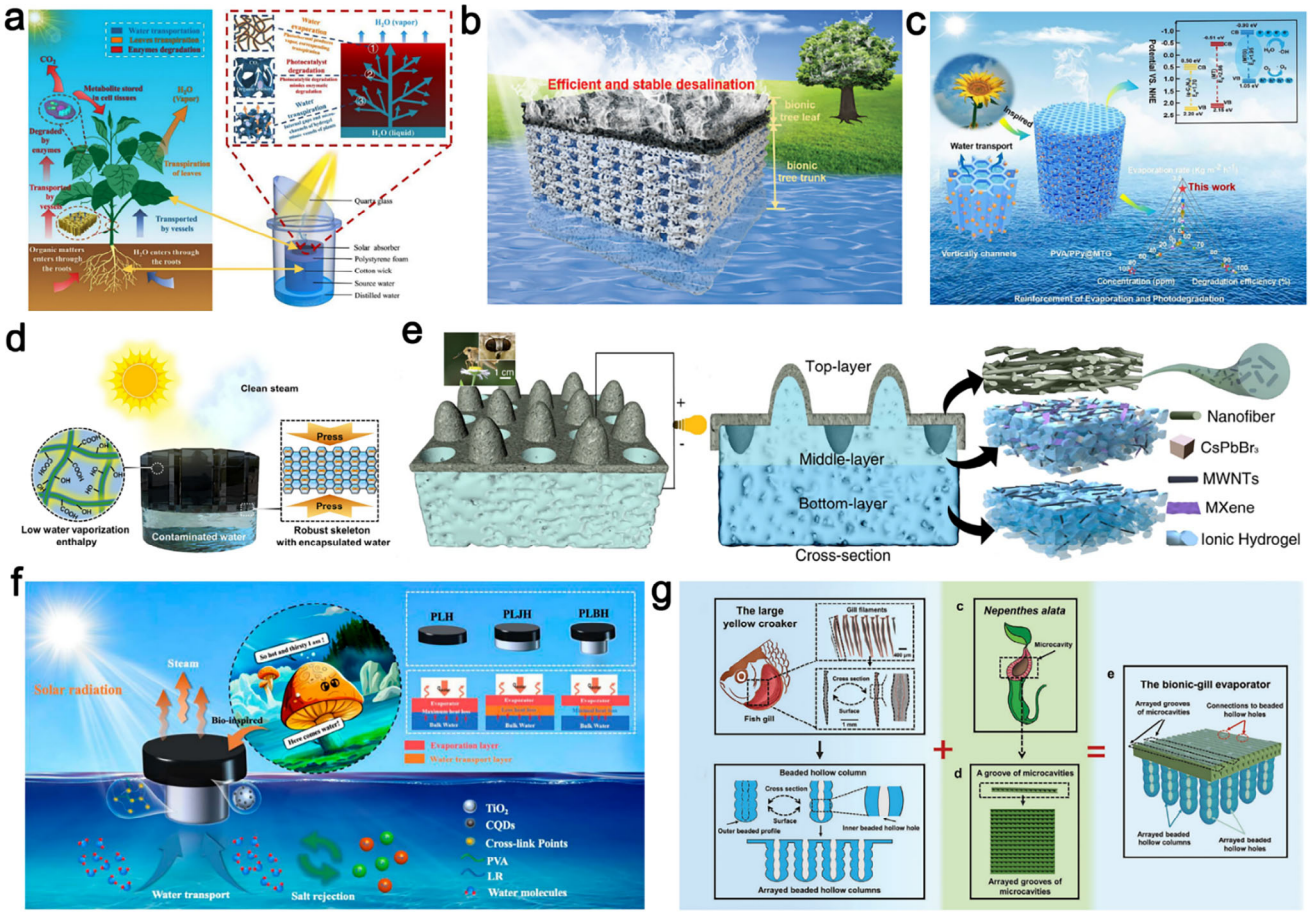


**Figure 13.** a) The schematic diagram of the plant and the bionic system. Reproduced with permission.[83] Copyright 2022, Elsevier. b) Schematic of the 3D-printed bionic hydrogel evaporator for efficient and stable solar desalination. Reproduced with permission.[84] Copyright 2024, Wiley-VCH. c) Schematic diagram of sunflower-inspired hydrogel evaporator. Reproduced with permission.[85] Copyright 2024, Elsevier. d) Schematic illustration of the sunflower-pith-based hydrogel-like solar evaporator. Reproduced with permission.[86] Copyright 2024, Elsevier. e) Moth-eye bionic hydrogel evapoartors. Reproduced with permission.[87] Copyright 2022, Springer Nature. f) Schematic diagram of the bionic mushroom-structured hydrogel evaporator desalination mechanism. Reproduced with permission.[88] Copyright 2023, Elsevier. g) Porcupine and gill-inspired salt-resistant evaporator. Reproduced with permission.[89] Copyright 2023, Wiley-VCH.

hierarchical pore structures, which amplify light-harvesting capabilities and localized photothermal conversion efficiency, synergize with biomimetic water-transport channels that enable rapid directional fluid transport via capillary forces coordinated with hydrophilic hydrogel networks, thereby reducing evaporation enthalpy. Concurrently, gradient wettability interfaces, which effectively suppress thermal dissipation while modulating vapor escape pathways are integrated with biofouling-resistant surfaces mimicking the lotus leaf's superhydrophobic/hydrophilic compartmentalization that effectively retard salt crystallization. The incorporation of biomimetic designs established a promising pathway for the advancement of PISSG technology.

### *3.1.3. The Regulation of Evaporation Enthalpy*

Water molecules exhibit polarity mainly because of the asymmetric distribution of charge between the O and H atoms. This inherent asymmetry enables the formation of hydrogen bonds, which promote intermolecular attraction (**Figure 14a**). During the PISSG process, water molecules must overcome the intermolecular forces generated by these hydrogen bonds to transition from the liquid to the steam phase, a process known as escaping (Figure 14b). By modulating both the number and strength of hydrogen bonds among water molecules, it becomes possible to effectively regulate the energy required to break these bonds, thereby controlling the enthalpy of evaporation.[90] A higher enthalpy of evaporation restricts the ER, consequently limiting both the steam generation rate and evaporation efficiency. Therefore, reducing the enthalpy of evaporation is crucial for accelerating its rate.[16] This reduction is intrinsically achieved by weakening or breaking hydrogen bonds, which lowers the energy barrier for water evaporation and thus accelerates the process. Since the hydrogen bond interactions between water molecules and other substances determine water's physical state, adjusting the enthalpy of evaporation emerges as a central strategy for improving evaporation efficiency.

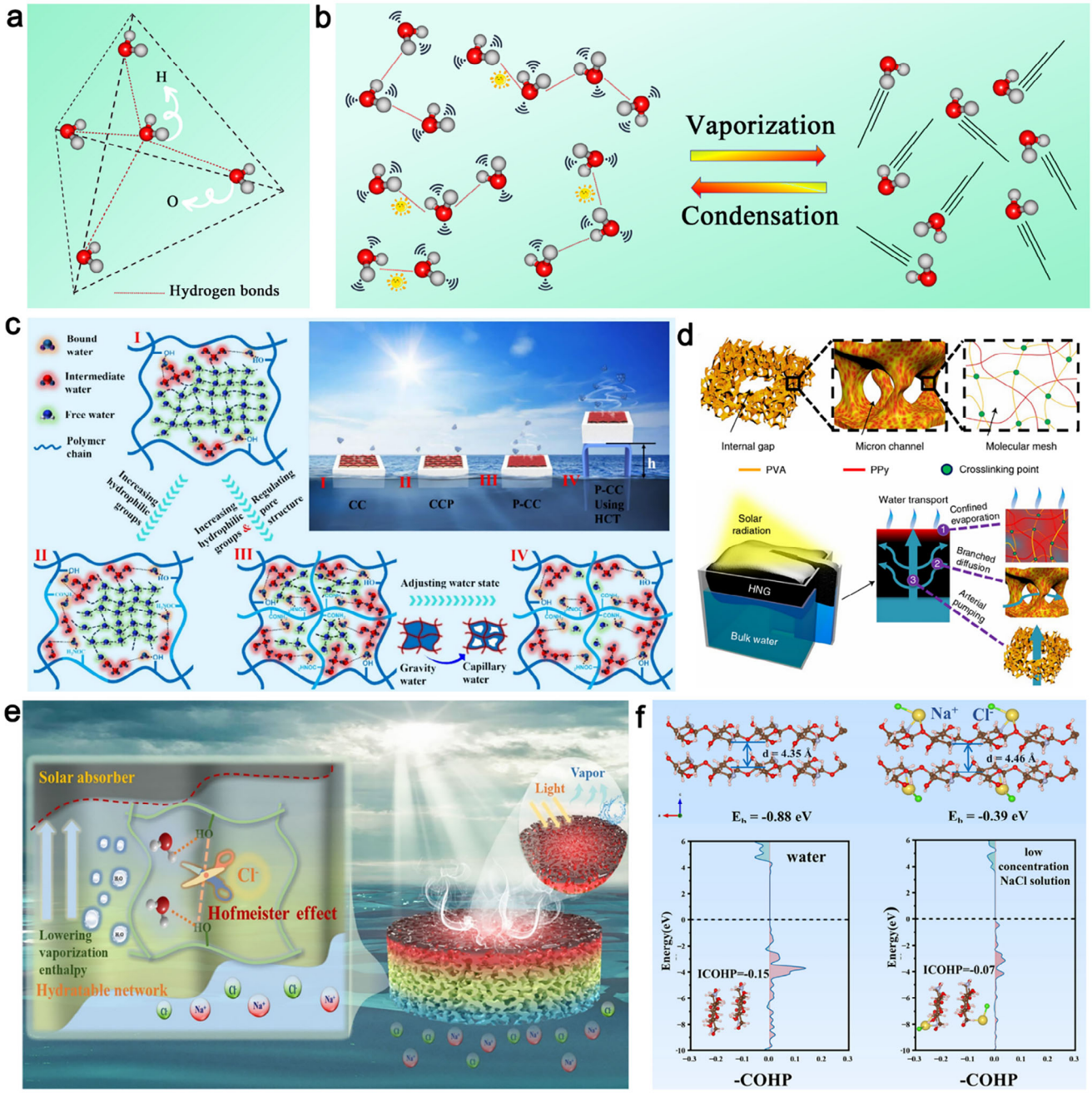


**Figure 14.** a) Molecular structure of $H_2O$. b) A dynamic hydrogen bonding network for condensation reforming of $H_2O$ molecules. c) Schematic illustration of reducing evaporation enthalpy through regulation of hydrophilic groups. Reproduced with permission.[91] Copyright 2025, Elsevier. d) Schematic of highly efficient solar vapor generation based on porous materials. Reproduced with permission.[92] Copyright 2018, Springer Nature. e) Schematics of the evaporator through the Hofmeister Effect. f) Theoretical simulations DFT calculations. Reproduced with permission.[93] Copyright 2025, Elsevier.

Water commonly exists in three distinct phases: solid (ice), liquid, and gas (steam), and each is characterized by a unique hydrogen bond network. During evaporation, a substantial number of hydrogen bonds are broken, facilitating the transition of water molecules from the liquid phase to isolated gaseous molecules. Conversely, condensation involves the reformation of these dynamic hydrogen bond networks. In hydrogel-based interfacial evaporators, the state of water is further categorized into bound water, intermediate water, and free water. Among these, intermediate water, which possesses relatively weaker hydrogen bonds and requires the least energy to break, predominantly contributes to the ER. Typically, the following strategies are employed to enhance evaporation efficiency:

1) **Introducing hydrophilic functional groups:** Xue et al. successfully reduced the evaporation enthalpy through a synergistic approach that involved optimizing hydrophilic groups, fine-tuning the pore network structure, and modifying the

interfacial water state within the cellulose/chitosan gel (Figure 14c).[91] Hydrophilic functional groups such as -OH, amino, and amide moieties contribute to the reduction of intermolecular hydrogen bonds among water molecules and increase the proportion of intermediate water (intermediate water/free water = 0.08). These modifications, combined with a hierarchical pore structure to optimize water transport pathways, synergistically decrease the evaporation enthalpy from the original 2450 kJ $kg^{-1}$ of pure water to 786 kJ $kg^{-1}$. This approach provides a theoretical foundation for the reduction of evaporation enthalpy.

2) **Constructing porous materials:** Yu et al constructed an evaporator based on PVA and polypyrrole. The enthalpy of evaporation for steam produced by high-temperature gas was notably decreased to 1765 kJ $kg^{-1}$ due to the formation of a hierarchical structure and the existence of liquid water clusters within the vapor phase (Figure 14d).[92] The porous structure adsorbs a large number of water molecules and forms water clusters, breaking the hydrogen bonds on the surface with less energy required and lower evaporation enthalpy than a single water molecule during evaporation. Besides, porous materials possess high porosity, providing a large evaporation area to promote water evaporation (3.2 kg $m^{-2}$ $h^{-1}$).
3) **Utilizing the Hofmeister effect:** Inspired by the Hofmeister effect, Bai et al. developed a highly hydratable network hydrogel evaporator that achieves a superior ER in brine compared to pure water (Figure 14e).[93] In this study, the Hofmeister effect, mediated by $Cl^-$ ions, modulates the microstructure of chitosan hydrogels by increasing the proportion of intermediate water (intermediate water/free water = 0.49) and weakening hydrogen bond strength. Density functional theory (DFT) calculations reveal that the presence of $Cl^-$ ions increases the interchain spacing of chitosan from 4.35 to 4.46 Å, thereby weakening the interchain hydrogen bonds, as indicated by the −COHP values rising from −0.15 to −0.07 (Figure 14f). The synergistic interaction among ions, polymer chains, and water molecules, mediated by the Hofmeister effect, lowers the energy barrier for water molecule escape, consequently reducing the thermodynamic enthalpy required for evaporation (1397 kJ $kg^{-1}$). The synergistic implementation of these strategies effectively improves interfacial evaporation performance.

### 3.2. Photothermal Conversion Mechanism

The efficiency of photothermal conversion ($\eta$) in hydrogel evaporators can be determined through the equations provided below:

$$\eta = \frac{m\left(h_v + Q_1\right)}{P_0} \tag{1}$$

$$Q_1 = C\left(T - T_1\right) \tag{2}$$

where $m$ represents the difference between the ER of the hydrogel under one sun irradiation and its ER in a dark environment; hv denotes the change in enthalpy of water between the gas and liquid phases; $Q_1$ indicates the sensible heat per unit mass of water; $P_0$ represents the power of the incident light; $C$ refers to the specific heat capacity of water (≈4.2 J $g^{-1}$ $°C^{-1}$); T is the temperature at which evaporation of the water occurs; and $T_1$ marks the initial temperature of the water.

The improvement of the conversion of hydrogel fundamentally relies solely on the efficient capture of light and the release of thermal energy by photothermal catalysts, as well as the optimized regulation of energy transfer and utilization by the hydrogel matrix. Through molecular design, structural engineering, and functional synergy, these two components collectively achieve high efficiency in photothermal conversion. The following discussion systematically elaborates on the mechanistic role of photothermal catalysts and the synergistic functionality of the hydrogel matrix. Photothermal catalysts serve as the "energy engine" for photothermal conversion, and their type and mechanism directly determine the energy conversion efficiency of the system.[94] Based on material characteristics, photothermal catalysts can be categorized into three types:

1) **Semiconductor Materials:** The photothermal conversion mechanism of semiconductor-based photothermal catalysts is primarily based on photo-induced bandgap charge excitation and electron-phonon interactions.[95] When semiconductor materials (e.g., $MoS_2$, CuS) are irradiated with light of specific wavelengths, electrons transition from the valence band (VB) to the conduction band (CB), forming electron-hole pairs. Subsequently, the energy is released as heat through non-radiative relaxation processes, such as lattice vibrations (**Figure 15a**).[96] Defect engineering is a critical strategy for enhancing photothermal conversion efficiency. The introduction of defects and thermal activation can reduce charge recombination, thereby improving light harvesting, charge carrier generation, and reactant adsorption.[97] Additionally, nonmetal doping synergizes with defect engineering to further extend the light absorption range and reduce the energy required for defect formation. Metal nanoparticles loaded on the semiconductor surface can enhance light absorption, prolong charge carrier lifetime, and provide additional active sites.[98] When the photon energy is sufficiently high, electrons are injected from the semiconductor's CB into the metal, where the metal acts as a cocatalyst to promote charge separation. Conversely, when the photon energy is below the semiconductor's bandgap, plasmon-mediated electron transfer occurs from the metal to the semiconductor. These mechanisms collectively optimize the photothermal conversion performance of semiconductor-based photothermal catalysts.
2) **Carbon-based materials:** The efficient photothermal conversion mechanism of carbon-based materials (such as GO and CNTs) primarily relies on the broad-spectrum absorption characteristics (200–2500 nm) of their conjugated $\pi$-bonds and their low thermal diffusivity.[99] When light irradiates the surface of carbon-based materials, their conjugated $\pi$-electron systems are excited, generating high-energy electron-hole pairs. As a result, the electrons in the excited state dissipate energy as heat via non-radiative relaxation mechanisms, including electron-phonon interactions.[100] Additionally, the elevated thermal conductivity and significant specific surface area of carbon-based materials enhance the efficiency of rapid heat transfer and promote a uniform distribution (Figure 15b).[101] For example, GO demonstrates excellent

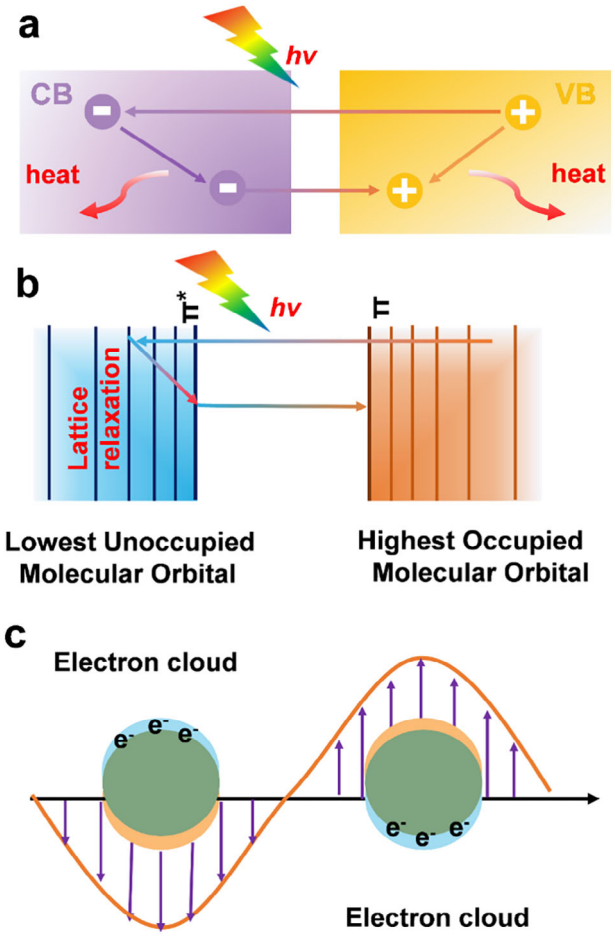


**Figure 15.** Mechanisms of photothermal effect with a) semiconductor materials, b) carbon-based materials, and c) metal nanoparticles.

photothermal conversion performance under near-infrared light due to its abundant oxygen-containing functional groups and defect structures, while CNTs achieve efficient light absorption and thermal conduction owing to their 1D nanostructure and $sp^2$-hybridized carbon network. Through chemical modification or heteroatom doping (e.g., nitrogen or sulfur doping), the band structure of carbon-based materials can be further tuned to enhance light absorption capacity and reduce electron-hole recombination rates, thereby significantly improving photothermal conversion efficiency. These properties make carbon-based materials highly promising for applications in solar energy utilization.

3) **Metal nanoparticles:** Metal nanoparticles, which possess a high polarizable density, exhibit strong interactions with electromagnetic radiation, such as surface-enhanced plasmonic effects.[102] Due to their unique optical properties, when the frequency of incident light resonates with the vibrational frequency of free electrons on the surface of noble metal nanoparticles, resonance is generated on their surface, leading to a significant increase in the collective vibration of surface electrons and the formation of localized electromagnetic field enhancements. The energy is then converted into thermal energy through non-radiative decay (e.g., electron-phonon collisions), resulting in the localized surface plasmon resonance (LSPR) effect. The LSPR on the surface of metal nanoparticles causes a substantial enhancement of the near-field intensity, leading to thermal localization around the nanoparticles (Figure 15c). Since the LSPR effect of metal nanostructures is closely related to the type, morphology, size, dielectric layer or medium, and assembly state of the nanoparticles, it is possible to prepare photothermal conversion materials with specific absorption wavelengths by manipulating the morphology and size of metal nanoparticles.[103] To date, Au and Ag nanoparticles are the most commonly used materials in photothermal applications. Ag demonstrates a notable plasmonic resonance with minimal losses within the optical frequency spectrum, while Au is well-known for its plasmonic resonance in the visible to near-infrared range, along with its excellent chemical stability.[104] In recent developments, various metals, including Al, Pd, and Pt, have emerged as promising candidates for a diverse array of plasmonic applications. The inherent characteristics of LSPR result in metal-based plasmonic nanoparticles demonstrating one or more distinct wavelength absorption peaks. This behavior constrains their overall effectiveness in the process of solar-thermal conversion. In general, diminishing the symmetry of a shape or designing hollow structures can enhance the LSPR bandwidth. Additionally, variations in particle size or alterations in the surrounding medium can lead to shifts in the LSPR band, as well as a corresponding widening of the absorption spectrum to some degree.[105]

The hydrogel matrix synergizes with photothermal catalysts to facilitate structural design and energy management. The 3D network structure of the hydrogel not only provides a loading platform for photothermal catalysts but also optimizes energy transfer and utilization efficiency through the following characteristics: 1) Hydrophilicity and water transport regulation. The microchannel water transport capability of hydrogels is crucial for photothermal evaporation and thermal management. The -OH and -COOH in natural polymers form hydrogen bonds with water molecules, creating directional water transport channels.[37] 2) Thermal localization and energy conservation. Thermal localization and energy conservation are critical aspects of photothermal applications. These objectives are effectively achieved through the hydrogel's low thermal conductivity matrix and high water content, which significantly restrict heat diffusion. Additionally, optimizing the photothermal interface, such as surface roughening or biomimetic structural design, can further enhance the light absorption efficiency, thereby promoting thermal localization and energy conservation. 3) Stimulus responsiveness and dynamic regulation. The thermosensitive phase transition properties of hydrogels, which enable dynamic modulation of energy utilization processes, are exemplified by thermosensitive PNIPAM hydrogels. These hydrogels undergo volume contraction at a critical temperature (LCST ≈ 32 °C), and when combined with photocatalysts, their ER under illumination can be significantly enhanced.[106]

The synergy between photothermal materials and the hydrogel matrix leverages the efficient light absorption capabilities of photothermal agents and the microchannel water transport properties of hydrogels. This combination not only reduces thermal

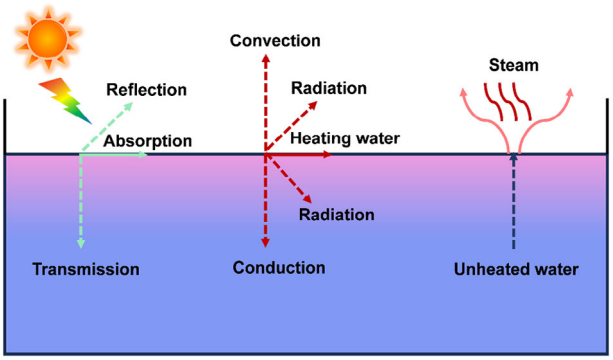


**Figure 16.** Schematic of the heat loss modes during the PISSG process.

diffusion losses but also dynamically regulates the evaporation process through thermosensitive hydrogels. Additionally, the low thermal conductivity matrix of the hydrogel, which ensures stable performance under high-salinity and high-temperature conditions, enables the photothermal conversion system to demonstrate efficient and sustainable advantages in the field of seawater desalination.

### 3.3. Thermodynamics and Interfacial Evaporation

The dynamic transfer of thermal energy during evaporation and the formation of the water-vapor interface are complex processes that encompass thermodynamics, fluid mechanics, and interface science. The subsequent discussion will focus on these two aspects.

#### *3.3.1. Dynamic Transfer of Thermal Energy*

In the process of PISSG, thermal energy is transferred mainly through the following ways (**Figure 16**):

1) **Thermal conduction:** Thermal conduction in the process of PISSG is a complex phenomenon involving the coupling of thermal transfer and phase transition. The core of this process is that heat is transferred from the inside of the liquid to its surface through the thermal conduction mechanism. This transfer drives the liquid molecules to absorb latent heat and convert it into vapor.[90] The basic law of thermal conduction is described by Fourier's law, which is heat flux.

$$q = -k\frac{dT}{dx} \tag{3}$$

where $q$ is the rate of heat transfer rate of per unit area, $k$ is the thermal conductivity of the liquid, dT/dx is the temperature difference of water before and after the illumination of the sun. In the process of evaporation, a temperature gradient is formed within the liquid due to heating or external heat sources. Heat is transferred from the high-temperature area to the low-temperature region (the liquid surface). As the liquid surface absorbs latent heat during evaporation, its temperature is usually lower than that of the liquid inside, which further exacerbates the formation of the temperature gradient. The heat conduction at the interface is closely coupled with the evaporation process to satisfy the heat equilibrium relationship:

$$q_{conduction} = q_{evaporation} \tag{4}$$

where $q_{conduction}$ is the heat transferred to the interface through heat conduction, and $q_{evaporation}$ is the heat required for the evaporation process. This means that the heat conducted at the interface is equal to the heat required for evaporation. The factors affecting the heat conduction efficiency include the thermal conductivity, temperature gradient, ER, and interfacial thermal resistance of the liquid, which is mainly caused by the molecular dynamic behavior and phase transformation process at the interface. To quantitatively study this process, mathematical models are often built in combination with heat transfer equations and interface conditions, while numerical simulation methods such as computational fluid dynamics or finite element analysis are employed to simulate the temperature distribution and heat conduction behavior. However, there are still challenges in practical applications, such as inhomogeneous temperature fields, interfacial dynamics, and multi-scale problems. To enhance heat conduction efficiency, optimization can be achieved by increasing the thermal conductivity of the liquid, optimizing the temperature gradient, or minimizing the interfacial thermal resistance.

2) **Thermal convection:** Thermal convection during the PISSG process, one of the key mechanisms of heat transfer, involves fluid motion induced by temperature gradients and plays a significant role in enhancing the evaporation process.[107] Thermal convection is categorized into two main types: natural convection and forced convection. Natural convection arises from density variations induced by temperature differences, whereas forced convection is propelled by external influences like airflow or mechanical agitation.[108] During the evaporation process, the liquid surface undergoes evaporative cooling, creating a temperature gradient where the lower, warmer liquid with lower density flows upward, while the upper, cooler liquid with higher density flows downward, thereby forming a natural convection cycle.[109] The heat transfer rate of thermal convection follows Newton's law of cooling, expressed as:

$$q = h\Delta T \tag{5}$$

where $q$ is the heat flux density, $h$ is the convective heat transfer coefficient, and ΔT is the temperature difference between the fluid and the interface.[110] Thermal convection in PISSG is characterized by temperature-gradient-driven flow, enhanced flow at the interface, and unsteady flow, the intensity of which is influenced by factors such as temperature gradients, liquid properties, interfacial conditions, and external airflow. Thermal convection is intrinsically coupled with the evaporation process. The evaporative cooling effect drives natural convection, while the resulting convective flow reciprocally enhances heat transfer to the interface and removes vapor molecules. This mechanism reduces interfacial vapor

pressure, thereby creating a positive feedback loop that further accelerates evaporation.[111] Numerical simulations, such as computational fluid dynamics, are widely used to visualize flow and temperature distributions, providing valuable insights into this process. To enhance the efficiency of thermal convection, natural convection can be strengthened by optimizing heating methods, and forced convection can be intensified by utilizing external airflow. Additionally, flow behavior can be optimized through interfacial engineering, such as surface modification.

3) **Thermal radiation:** Thermal radiation, which refers to the process of heat transfer through electromagnetic waves (primarily in the infrared spectrum) between a liquid surface and the surrounding environment, is described by the Stefan-Boltzmann law, expressed as:

$$q_{radiation=}\epsilon\sigma(T_s^4 - T_\infty{}^4) \tag{6}$$

where $q$ is the radiative heat flux density, $\epsilon$ is the surface emissivity (a parameter that characterizes the surface's ability to emit radiation and ranges between 0 and 1), $\sigma$ is the Stefan-Boltzmann constant ($5.67 \times 10^{-8}$ W m$^{-2}$ K$^{-4}$), $T_s$ represents the absolute temperature of the liquid surface, and $T_\infty$ is the absolute temperature of the surrounding environment.[90,112] In PISSG systems, thermal radiation exhibits three defining characteristics: non-contact heat transfer, a fourth-power temperature dependence, and pronounced sensitivity to surface emissivity. Meanwhile, its intensity is governed by multiple interacting parameters, including liquid surface temperature, ambient temperature, surface emissivity, and surface properties. These collective parameters modulate radiative energy exchange, thereby establishing dynamic coupling between thermal radiation and evaporation efficiency.[111] Thermal radiation, which is closely coupled with the evaporation process, not only provides additional heat to the liquid surface to promote evaporation but also indirectly regulates the ER by influencing the temperature distribution.

#### *3.3.2. Formation of the Water-Steam Interface*

In the process of PISSG, the formation of the water-vapor interface is a dynamic and complex phenomenon. The molecules at the liquid surface absorb thermal energy to increase their kinetic energy and escape into the vapor phase when their kinetic energy is sufficient to overcome intermolecular forces and surface tension. This process is described by the Clausius-Clapeyron equation:

$$\frac{dP}{dT} = \frac{L}{T\left(V_g - V_l\right)} \tag{7}$$

where $P$ represents the vapor pressure, $T$ denotes the temperature, $L$ signifies the latent heat, and $V_g$ and $V_l$ correspond to the molar volumes of the vapor and liquid phases, respectively.[113] At the interface, a dynamic equilibrium is formed between the escaping liquid molecules and the condensing vapor molecules. The thickness of the interfacial layer, which varies with the ER, impacts the efficiency of heat and mass transfer.[114] Surface tension, which plays a critical role in interface formation by minimizing the liquid surface area and influencing the shape and stability of the interface, can lead to interface fluctuations or the formation of microstructures (such as droplets or vapor bubbles) when it varies.[115] The vapor molecules escaping from the liquid surface diffuse into the surrounding environment through diffusion and convection, with the diffusion rate described by Fick's law:

$$J = -D\frac{dC}{dx} \tag{8}$$

where $J$ denotes the diffusion flux, $D$ signifies the diffusion coefficient and dC/dx refers to the concentration gradient.[116] At the interface, heat and mass transfer, which are closely coupled, jointly determine the ER. Heat transfer provides the latent heat required for evaporation, while mass transfer occurs through vapor diffusion and convection. In practical applications, the interface formation process, which can be regulated through surface modification (such as chemical coatings or physical treatments), external condition control (such as adjusting temperature, pressure, or airflow velocity), and microstructure design (such as nanopillars or microchannels), is optimized to enhance evaporation efficiency.

The dynamic transfer of heat energy during the evaporation process and the formation of the water-vapor interface represent a multidisciplinary research field. By gaining an in-depth understanding of this process, relevant technical optimizations and an important theoretical basis can be achieved for advancing seawater desalination and energy utilization.

## 4. Applications

The recent rapid advancement of evaporation technologies has resulted in a significant increase in ER and enhanced energy conversion efficiency. This holds great promise for various applications aimed at promoting sustainability in water and energy. From a practical perspective, we highlight the most potential applications and present the latest developments in solar water evaporators in the following section. These advancements include seawater desalination, water purification, photocatalytic degradation, and the harvesting and utilization of energy.

### 4.1. Seawater Desalination

The total 97% of the global water exists as seawater, which is unsuitable for drinking. This means that only 3% is freshwater and available for human consumption. The challenge of water scarcity can be addressed by converting seawater into freshwater. The effectiveness of desalination technology depends on factors such as ER, sustainability, and environmental compatibility. The ER is directly related to freshwater output and serves as the most crucial parameter for evaluating the efficiency of the desalination process. Traditional desalination methods, such as pressure steam distillation, multi-stage flash distillation, and reverse osmosis technologies, can basically meet the daily freshwater demands of individuals. However, those methods require high power consumption, large centralized installations, and frequent maintenance. Hydrogel-based photothermal evaporators,

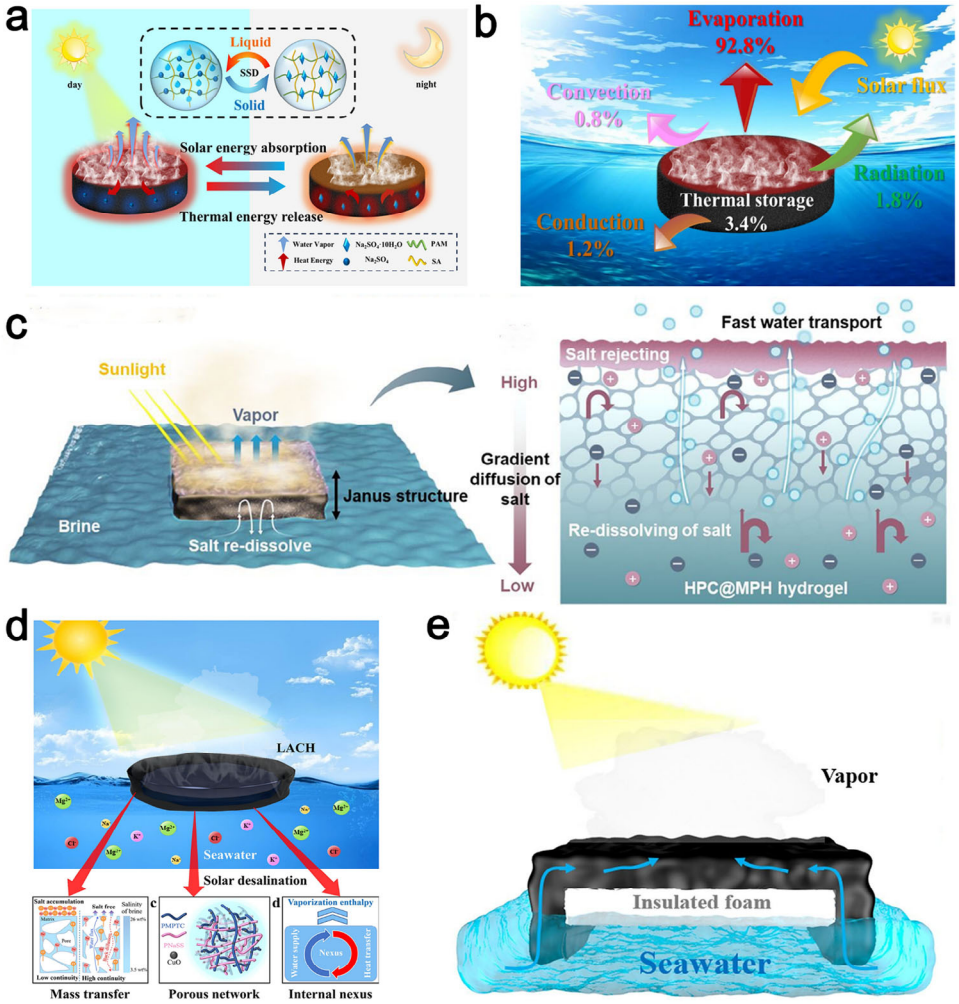


**Figure 17.** a) A schematic representation showcasing the process of PISSG utilizing hydrogel-integrated phase change materials. b) The energy analysis of the evaporator. Reproduced with permission.[117] Copyright 2025, Elsevier. c) Mechanism of efficient salt resistance of the HPC@MPH hydrogel. Reproduced with permission.[27] Copyright 2025, The Royal Society of Chemistry. d) The schematic of solar desalination of LACH. e) Schematic of the LACH-based evaporator for seawater desalination. Reproduced with permission.[118] Copyright 2024, Elsevier.

which are driven by natural sunlight, have attracted considerable interest because of their remarkable potential to produce freshwater from seawater in a low-cost and environmentally sustainable manner, thereby supporting global zero-carbon initiatives.

Li et al. prepared a dual-network hydrogel composed of SA and PAM, which exhibited an ER of 2.72 kg $m^{-2}$ $h^{-1}$ under one sun radiation (**Figure 17**a,b).[117] Furthermore, even without solar radiation, the ER is consistently maintained at 1.25 kg $m^{-2}$ $h^{-1}$, which signifies a 16.8% enhancement in freshwater output when compared to hydrogels that do not incorporate phase change materials. In addition, Liang et al. developed a material in this study that is based on a thermos-responsive hydroxypropyl cellulose (HPC) and MXene photothermal conversion unit, demonstrating significant potential for solar-driven seawater desalination (Figure 17c).[27] The Janus hydrogel absorber achieves an ER of 3.11 kg $m^{-2}$ $h^{-1}$ under one sun irradiation. In simulated seawater (3.5 wt.% NaCl), the material, which maintains a stable ER of ≈2.58 kg $m^{-2}$ $h^{-1}$, demonstrates remarkable long-term stability over 30 h of continuous solar desalination. In real seawater (Bohai Sea, China), the material achieves an ER of 2.55 kg $m^{-2}$ $h^{-1}$, demonstrating performance comparable to that in simulated seawater. Under natural sunlight conditions, the material, which exhibits a total evaporation of 9.59 kg $m^{-2}$ over 8 h, demonstrates stable performance in complex environments. After 100 h of cyclic testing, the material, which maintains a stable ER of ≈2.95 kg $m^{-2}$ $h^{-1}$, exhibits excellent durability for practical applications.

Moreover, An et al. developed an ion-engineered copper-based hydrogel photothermal evaporator (LACH) that integrates oppositely charged polymer chains (4-Vinylbenze-nesulfonic acid sodium salt and [3-(methacryloylamino)propyl]-trimethy-lammonium chloride solution) as the substrate with CuO nanoparticles exhibiting LSPR effects as the photothermal conversion layer (Figure 17d).[118] This rationally designed architecture, which synergizes ionic engineering with plasmonic photothermal conversion, enables high-efficiency solar desalination while

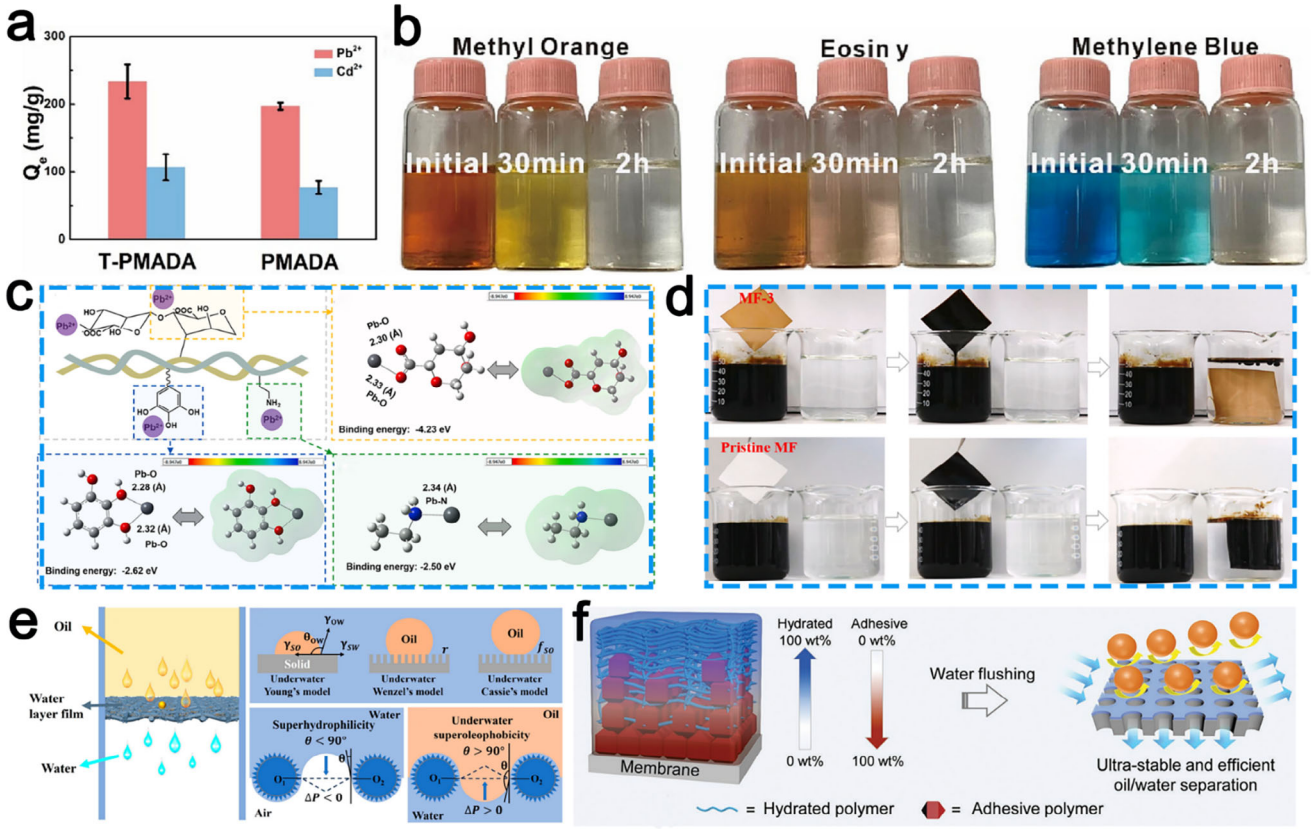


**Figure 18.** a) Heavy metal ions adsorption ability. b) The photos of catalytic degradation of methyl orange, eosin y, and methylene blue by T-PMADA hydrogel. Reproduced with permission.[119] Copyright 2023, Elsevier. c) The interactions between the functional groups of the synthesized nanocomposite hydrogel coating and $Pb^{2+}$ ions. d) The pictures of anti-crude oil-fouling behaviors. Reproduced with permission.[120] Copyright 2023, Elsevier. e) Schematic diagram showing the wetting models of the PAA/CS@$SiO_2$ coated mesh. Reproduced with permission.[121] Copyright 2024, The American Chemical Society. f) A diagram illustrating the membrane enhanced by the gradient adhesive hydrogel, designed for remarkably stable and effective separation of oil and water. Reproduced with permission.[122] Copyright 2022, Wiley-VCH.

achieving enhanced ER of 3.93 kg $m^{-2}$ $h^{-1}$ under one sun irradiation. Under outdoor natural light conditions, LACH produced a cumulative 10 kg $m^{-2}$ of freshwater during an 8-h test, which can meet the daily drinking water needs of two families (Figure 17e). The simple preparation process and excellent properties make it an ideal candidate material for large-scale desalination applications in the future. Hydrogel-based PISSG technology not only surpasses traditional seawater desalination technology in ER but also improves energy utilization, offers significant economic benefits, and is environmentally friendly. Such technology provides a new perspective and direction for addressing the problem of freshwater scarcity.

### 4.2. Wastewater Purification

In addition to seawater desalination, solar water evaporators hold significant potential for wastewater purification. Typically, the process of wastewater purification encompasses various aspects, including the degradation of organic dyes, the removal of heavy metal ions and VOCs, as well as the separation of emulsified water and oil mixtures. For example, Zhang et al. developed a porous hydrogel (T-PMADA), which was synthesized through the copolymerization of acrylic acid (AA) and methacrylamide dopamine (MADA) in conjunction with $Ti_3C_2$ MXene.[119] The porous structure provides abundant active sites for pollutant treatment. The T-PMADA evaporator demonstrates effective performance in the simultaneous removal of heavy metal ions and organic dyes when treating wastewater that contains these contaminants (**Figure 18**a,b). In addition, Shao et al. introduced a nanocomposite hydrogel-coated membrane that integrates tannic acid (TA), SA, and 3-aminopropyltriethoxysilane (APTES). This method integrates the strong adhesive properties of TA, the structured architecture facilitated by APTES, and the excellent hydration potential of SA.[120] The remarkable capacity for heavy metal adsorption can be attributed to the presence of plentiful adsorption sites, such as -$COO^-$, -$NH_2$, and phenolic hydroxyl groups, along with the extensive surface area offered by the hierarchical structures. The developed super wetting membranes demonstrate considerable potential for the purification of oil/water emulsions and the removal of heavy metal ions, effectively addressing environment remediation by the concept of "killing two birds by one stone" (Figure 18c,d). Guo et al. prepared hydrogel-coated mesh for oil/water separation. A dual-network hydrogel layer (PAA/CS@$SiO_2$) was developed by employing acrylic acid, chitosan, and modified silica, which

**Table 2.** Hydrogel evaporators for various wastewater purifications.

| Evaporators | Pollutants | Removal method | Efficiency | Refs. |
|---|---|---|---|---|
| T-PMADA | Pb (II) | adsorption | 609.9 mg/g | [119] |
| | Cd (II) | | 250.2 mg/g | |
| | methyl orange | photodegradation | 37.2% | |
| | eosin-Y | | 39.8% | |
| | methylene blue | | 45.1% | |
| APTES | Oil/water separation | adsorption | 96.7% | [120] |
| | $Pb^{2+}$ | | 64.6% | |
| PAA/CS@$SiO_2$ | Oil/water separation | adsorption | 99% | [121] |
| protocatechuic acid/hydrated calcium alginate | Oil/water separation | adsorption | 99.99% | [122] |
| $MoS_2$-PAM | methylene blue | photodegradation | 99% | [67a] |
| | $Ca^{2+}$ | adsorption | 99.6% | |
| | $K^+$ | | 98.8% | |
| | $Mg^{2+}$ | | 99.6% | |
| | $Na^+$ | | 99.3% | |
| | oil/water separation | | 94.8% | |
| polymerizing porous hydrogel | Methylene blue | photodegradation | 99% | [123] |
| | Rhodamine B | | | |

were photopolymerized onto stainless steel mesh. Subsequently, a novel and straightforward ultrasonic-assisted technique was applied to facilitate pore formation, resulting in the emergence of numerous in situ pores on the surface of the hydrogel-coated mesh. This development effectively enhanced the water flux while maintaining the separation efficiency (Figure 18e).[121] Moreover, Jin and colleagues developed gradient adhesive hydrogels decorated with super hydrophilic membranes to achieve a highly stable separation of oil and water.[122] The hydrogel membranes facilitate unparalleled stability and efficiency in separating surfactant-stabilized oil-in-water emulsions and crude oil/water mixtures, boasting an impressive cycling capability of ≈100% flux recovery along with negligible irreversible oil fouling (Figure 18f). This research introduces an innovative approach to the design of anti-oil-fouling membranes aimed at enhancing practical applications in oil/water separation. More hydrogel evaporators used in wastewater purification are shown in **Table 2**.

### 4.3. Photocatalytic Degradation

Integrating hydrogel-based solar evaporation with photocatalytic degradation offers a promising solution for producing clean water while effectively removing contaminants. Min et al. successfully developed a novel dual-functional hydrogel, integrating photothermal conversion with photocatalytic degradation capabilities (**Figure 19a**).[124] The developed evaporator demonstrates a commendable water ER of 2.22 kg $m^{-2}$ $h^{-1}$, along with an outstanding energy conversion efficiency of 92% when subjected to one sun irradiation. Additionally, it exhibits a photocatalytic degradation efficiency of 97% for methylene blue (MB) and 94% for tetracycline (TC). In practical applications, the evaporator functions as an outdoor unit designed to simultaneously facilitate the generation of freshwater while effectively eliminating pollutants (Figure 19b). This discovery enhances the development of sustainable and efficient water purification methods, offering important perspectives for future studies and practical applications.

In addition, Qu and coworkers developed a biomimetic hydrogel known as polypyrrole/foam-like carbon nitride/PVA (PCH) through a process of directional freeze-drying, which incorporates vertically aligned channels (Figure 19c).[125] The existence of vertically aligned channels not only minimizes heat loss and enhances energy conversion efficiency but also promotes the movement of water and organic contaminants toward the air-water interface. The final results indicate that the ER achieves 2.27 kg $m^{-2}$ $h^{-1}$ under one sun irradiation. Simultaneously, the TC degradation efficiency can achieve 90.6% in just 1 h. In an outdoor study, following 11 h of exposure to sunlight, the TC degradation efficiency and freshwater output of the PCH evaporator rose to 99.0% and 6.2 kg $m^{-2}$, respectively (Figure 19d,e). A novel black hydrogel composed of black g-$C_3N_4$, loofah, and chitosan (BCN/LF/CS) has been developed by Shi's research team, functioning as a highly efficient dual-function solar evaporator for both desalination and the degradation of antibiotics.[126] In a 3.5 wt.% NaCl solution, the optimal evaporator demonstrates an impressive effective ER of 2.1 kg $m^{-2}$ $h^{-1}$, while achieving a remarkable 91.4% degradation of TC solution within just 6 h (Figure 19f). This work paves the way for future exploration of photocatalysts and their diverse applications in photocatalysis degradation.

Moreover, Zhou et al. prepared a novel heterogeneous structure comprising iron-based metal-organic frameworks and multi-walled carbon nanotubes combined with a gelatin-PVA double network hydrogel (MMH).[107] MMH demonstrates an ER of 2.84 kg $m^{-2}$ $h^{-1}$, achieving an efficiency of 95.3% under one

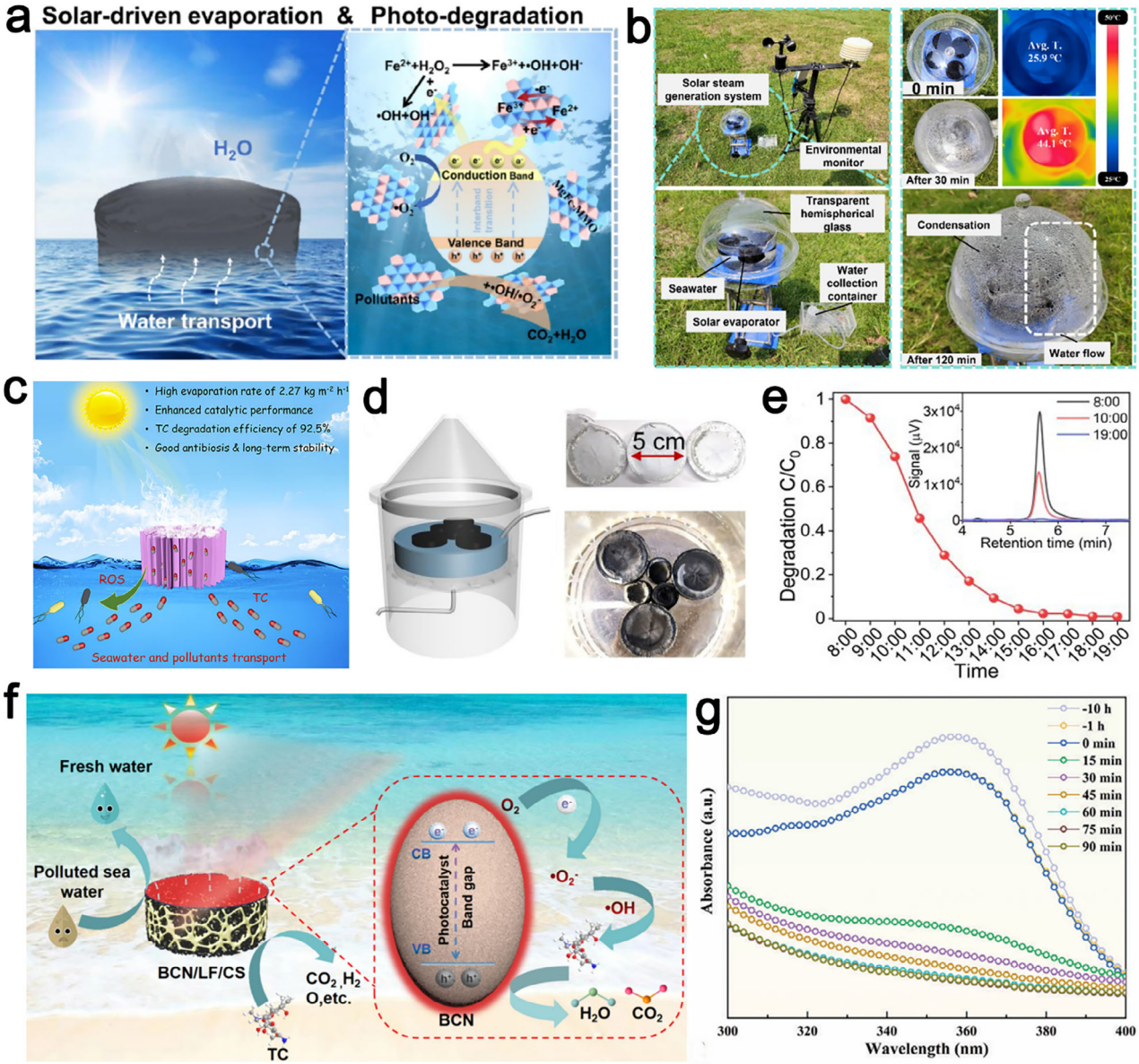


**Figure 19.** a) The solar-driven evaporation and photodegradation of the dual-function hydrogel. b) Images showcasing the outdoor device, along with IR images and photographs illustrating the device both prior to and following the evaporation process for outdoor experiments. Reproduced with permission.[124] Copyright 2024, Elsevier. c) Scheme illustrating the degradation of TC in contaminated water through evaporation-enhanced processes facilitated by vertical-channel hydrogels. d) Scheme of the device for outdoor solar evaporation. e) The degradation of TC with varying irradiation time. Reproduced with permission.[125] Copyright 2022, The American Chemical Society. f) Mechanism diagram of solar evaporator for desalination coupled with TC degradation. Reproduced with permission.[126] Copyright 2025, Elsevier. g) UV–vis curves of TC over different reaction periods in the presence of MMH evaporator. Reproduced with permission.[107] Copyright 2024, Wiley-VCH.

sun. Meanwhile, the three-phase interface significantly boosts thermal convection, effectively diminishing the barrier to gas release from the reaction system, and consequently enhancing the efficiency of the interfacial photothermal-photocatalytic process. For the removal of TC, MMH exhibited excellent TC degradation ability, achieving an 86.6% reduction within 90 min (Figure 19g). These articles reassess the critical role of thermal convection in interfacial photothermal-photocatalytic systems and provide unique insights into the design of hydrogel-based interfacial photothermal photocatalytic systems for solar energy conversion. More hydrogel evaporators used in photocatalytic degradation are shown in **Table 3**.

### 4.4. Energy Harvesting and Conversion

Hydrogel-based hygroscopic materials typically demonstrate superior moisture absorption performance owing to their compressible 3D polymeric network architecture.[131] Recently, efforts have been made to deploy hydrogels in various energy harvesting

**Table 3.** Represent the hydrogel evaporators used in photocatalytic degradation.

| Evaporators | Pollutants | Efficiency [1 h] | Refs. |
|---|---|---|---|
| g-$C_3N_4$/PVA/chitosan | methylene blue | 99.5% | [33] |
| CuS@MIL-100/cellulose hydrogel | methylene blue | 97.3% | [127] |
| | tetracycline | 93.3% | |
| PVA/PPy@MXene@$TiO_2$@g-$C_3N_4$ | VOCs (100 ppm) | 94.2% | [85] |
| g-$C_3N_4$/loofah/chitosan | tetracycline | 91.4% (6 h) | [126] |
| 3D GO/NPDI/PVA-rGO/PU/NPDI | ciprofloxacin hydrochloride | 74.04% | [128] |
| $Ti_3C_2$ MXene/CdS hydrogel | phenol | 85.12% | [129] |
| | metronidazole | 100% | |
| MF/CNTs-1 hydrogel | methylene blue | 97% | [124] |
| | tetracycline | 94% | |
| PCH | tetracycline | 90.6% | [125] |
| MMH | tetracycline | 86.6% (1.5 h) | [107] |
| MF/$TiO_{2-x}$/BiOI | Rhodamine B | 100% | [130] |

and conversion applications.[132] The driving force of the energy generation can be divided into the following two aspects:

1) Ion concentration gradient: Wang et al. developed a highly efficient hydrogel film for electricity generation. The SA–$SiO_2$–rGO hydrogel film produced demonstrates an impressive open-circuit voltage reaching ≈0.6 V, alongside a short-circuit current of ≈2.24 mA (0.14 mA $cm^{-2}$) (**Figure 20a**).[133] The fundamental principle underlying the generation of current and voltage in this evaporator primarily originated from the directional migration of ions due to the concentration gradient of ions. As water molecules gradually approach the power generation device, they will undergo dissociation reactions with the hygroscopic material, leading to the release of a substantial number of mobile protons from hydrophilic functional groups such as -OH and -COOH. Simultaneously, negatively charged functional groups remain immobilized due to their strong binding with the hygroscopic substrate. The directed movement of positively charged ions along the ion concentration gradient induces an electrical signal detectable in the external circuit, thereby enabling the output of electrical energy. This work provides a novel theoretical foundation and technical approach for the design and fabrication of composite materials with highly efficient electric energy conversion and advanced micro-scale power supply sensors, thereby driving innovative progress in the related fields.
2) Temperature gradient: A photosensitive janus ionogel was prepared by the synergism of the photothermal effect and thermoelectric effect by Chen's team (Figure 20b).[134] This ionogel demonstrates a Seebeck coefficient of 19.5 mV $K^{-1}$ and achieves a ZT value of 0.63 (Figure 20c). The temperature gradient drives the migration of cations and anions from the luminescent side (hot end) toward the non-luminescent side (cold end), resulting in an asymmetric distribution and accumulation of ions at both ends of the gel. This ionic imbalance induces significant voltage generation at the two electrodes due to ion-induced charge effects. Notably, the photosensitive Janus ion gel efficiently converts solar energy into electrical energy through a "light-heat-electricity" cascade conversion mechanism, effectively harnessing sunlight of varying intensities. This distinctive property highlights its promising potential for applications in solar energy harvesting and optical sensing technologies. Wong et al. proposed a novel strategy to use the surfactant Pluronic F127 to encapsulate carbon black, forming a size-stable "core-shell" nanomicelle photothermal hydrogel.[35] It can be used to generate electricity and facilitate the integration of outdoor evaporation of water and electricity generation. The area of large-scale surface patterning can reach 132 $cm^2$ (22 × 6 cm), and the output voltage under natural light can be as high as 561 mV (Figure 20d,e). This is due to the temperature difference between two distinct conductors or semiconductors, which induces a potential difference. The voltage generated by thermoelectric devices is linearly proportional to the temperature gradient. This work provides a valuable perspective on the industrialization of high-performance solar evaporators. Liu et al. prepared a hydrogel-based evaporator that consists of 0D carbon quantum dots (CQDs), 2D MXene, and sodium carboxymethyl cellulose (CMC)/PAM.[135] Expect a high ER of 1.93 kg $m^{-2}$ $h^{-1}$, the hydrogel evaporators are used for photothermal sensing and temperature difference power generation. It presents an efficient output power density of 230.7 mW $m^{-2}$ under one sun. This work provides a proof-of-concept for the design of multipurpose solar evaporation systems. Furthermore, hydrogel evaporators used in energy harvesting and conversion are shown in **Table 4**.

### 4.5. Sterilization

Steam sterilization is widely recognized as an effective and cost-efficient method for addressing bacterial contamination in drinking water. However, its reliance on electricity results in higher costs, thereby limiting accessibility for many individuals. Hydrogel-based solar steam evaporators, which utilize solar-driven water evaporation for sterilization, represent the most cost-effective and environmentally friendly technology for eliminating bacteria and viruses in drinking water. Li et al.

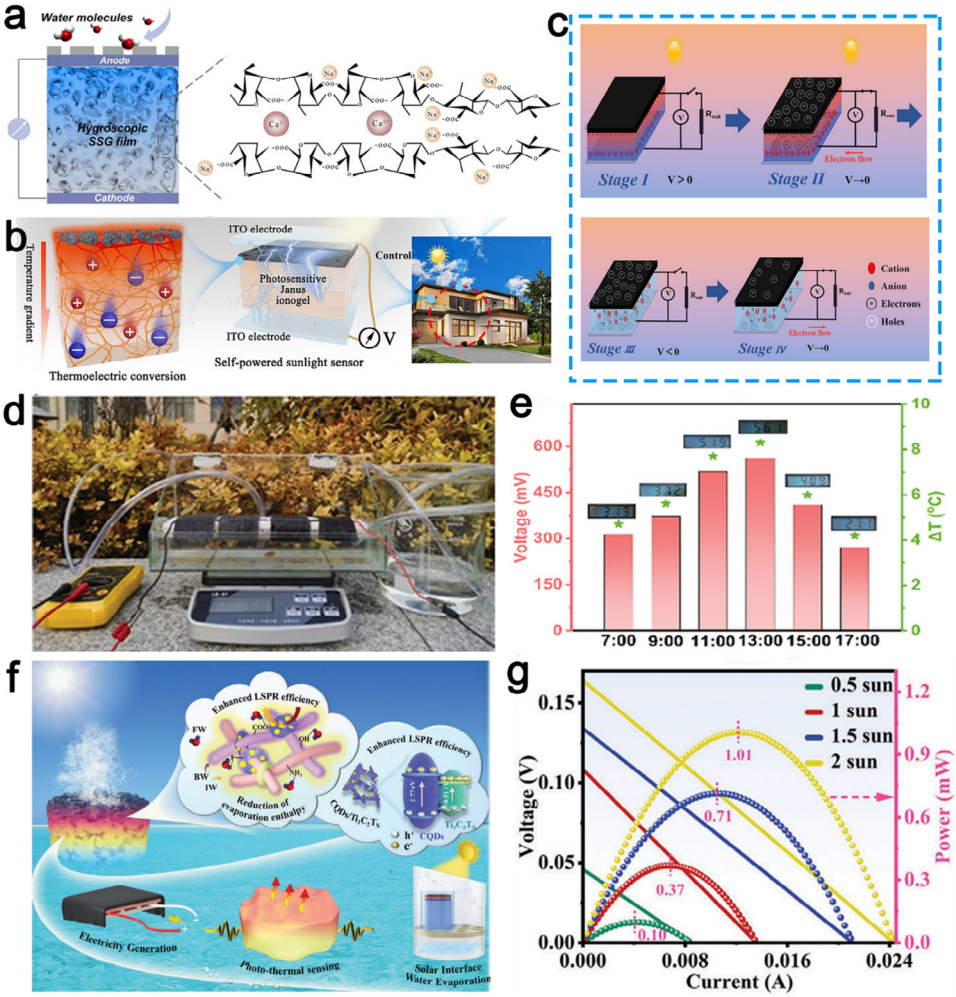


**Figure 20.** a) Moisture-induced electricity generation in the SMEG. Reproduced with permission.[133] Copyright 2024, Elsevier. b) The thermoelectric conversion mechanism of the underlying ionogel layer, along with the configuration of a self-powered solar intensity sensing device. c) A schematic representation depicting the operational principles of a photosensitive Janus ionogel-based capacitor is illustrated in four distinct stages. Reproduced with permission.[134] Copyright 2024, Elsevier. d) Photo of outdoor power generation experiment equipment under natural sunlight. e) Output voltage and temperature difference of evaporator surface under natural light recorded every 2 h. Reproduced with permission.[35] Copyright 2025, Wiley-VCH. f) Schematic diagram of photothermal hydrogel for solar water evaporation, photothermal sensing, and electricity generation. g) Power at different solar illumination. Reproduced with permission.[135] Copyright 2024, Wiley-VCH.

successfully developed a solar evaporator (SA/CCC/$Cu^{2+}$) by using a $Cu^{2+}$ crosslinked biomass SA hydrogel as the foundational structure, while incorporating carbonized carboxymethyl chitosan (CCC) as the internal photothermal material (**Figure 21a**).[143] As-developed evaporator exhibits an impressive ability to inactivate *Escherichia coli* (*E. coli*), achieving complete elimination of the bacteria within 40 min (Figure 21b). The final elimination of the bacteria can be attributed to the effect of $Cu^{2+}$, which binds strongly with the negatively charged bacterial cell wall, thereby blocking some of the bacteria's normal metabolic pathways. The high temperature hindered the activity of the bacterial cells and affected their metabolic function. Additionally, the reactive oxygen species produced by the photocatalysis of SA/CCC/$Cu^{2+}$ and $Cu^{2+}$ attacked the bacteria cell membrane, making the bacteria easier to eliminate.

In addition, He et al. developed a self-polymerizing porous hydrogel (PDIH) evaporator using a simple method similar to dough making, which exhibited excellent antibacterial properties (Figure 21c).[123] The remarkable antibacterial adhesion properties can be attributed to the presence of the -$N(CH^{+}{}_{3})_{2}$ group in the polymerization of [2-(methylpropenoxy) ethyl] dimethyl -(3-sulfopropyl) ammonium hydroxide. This functional group engages in electrostatic interactions with the anionic components of bacterial cell membranes, leading to a physical attack of the membrane structure (Figure 21d). It is anticipated that the development of such hydrogel evaporators will significantly advance sterilization technologies during steam generation. Yu et al. developed antibacterial hydrogels (ABHs) consisting of catechol-functionalized chitosan (CCS) network and quinone-anchored activated carbon particles for effective water treatment (Figure 21e).[144] The agar plates show the inactivation results of

**Table 4.** Recent performances of hydrogel evaporators in energy harvesting and conversion.

| Evaporators | Driving force | Energy generated | Efficiency | Refs. |
|---|---|---|---|---|
| SA–$SiO_2$–rGO hydrogel | ion concentration gradient | voltage | 0.6 V | [133] |
| | | current | 0.14 mA $cm^{-2}$ | |
| Acrylamide/3-sulfopropyl acrylate potassium salt | | power density | 13.73 W $m^{-2}$ | [136] |
| moisture-driven energy generator | | voltage | 1.20 V | [137] |
| | | current | 0.45 mA | |
| zwitterionic gradient double-network hydrogel membrane | | power density | 49.6 W $m^{-2}$ | [138] |
| polyanion hydrogel | | power density | 16.4 W $m^{-2}$ | [139] |
| moisture-activated electricity generator | | power density | 13.8 W $m^{-2}$ | [140] |
| janus ionogel | Temperature gradient | voltage | 65 mV | [134] |
| Pluronic F127 | | voltage | 561 mV | [35] |
| CMC/PAM | | power density | 230.7 mW $m^{-2}$ | [135] |
| PVA thermoelectric generator | | power density | 1.02 W $m^{-2}$ | [141] |
| bis[2-(methacryloyloxy)ethyl] phosphate | | power density | 11.53 W $m^{-2}$ | [142] |

*Bacillus subtilis* (*B. subtilis*), *E. coli*, and *Pseudomonas aeruginosa* (*P. aeruginosa*) cells, demonstrating the effectiveness of water disinfection by ABHs at room temperature and ambient pressure (Figure 21f). The bactericidal effect is attributed to the synergy between hydrogen peroxide and quinone groups, which attack essential cell components and disrupt bacterial metabolism. In addition, by utilizing the benefits of stable chemical modifications and crosslinking techniques, hydrogels can integrate two antibacterial elements: catechol groups and quinone-activated carbon particles. These components are largely inert in aqueous environments and demonstrate minimal oxidation effects. Consequently, they are anticipated to generate no harmful byproducts or residual substances. The ABH platform provides a more efficient solution for point-of-use water treatment technologies, significantly reducing energy and chemical requirements, particularly in remote areas and emergency rescue applications. More sterilization performances of hydrogel evaporators are shown in **Table** 5.

## 5. Conclusion and Prospective

Due to the relentless dedication of various research teams across the globe, the hydrogel-based photothermal interfacial evaporator, as an emerging, cost-effective, clean, and renewable energy-powered water purification reactor, has made significant advancements over the past years. This review introduces hydrogel-based evaporators with different substrates, highlighting their merits and the practical necessity for the development of PISSG technology. Subsequently, it thoroughly analyzes crucial properties of hydrogels affecting the evaporation efficiency of PISSG, detailing the photothermal conversion mechanism of photothermal catalysts and hydrogels, and introducing the dynamic transfer of thermal energy as well as the process of the forming of the water-vapor interface. In addition, diverse applications of hydrogel-based evaporators are outlined, extending beyond conventionally recognized fields such as seawater desalination, wastewater purification, photocatalytic degradation, multiple energy harvesting and conversion, and sterilization. Furthermore, the challenges and perspectives of hydrogel-based evaporators are elucidated, aiming to fully demonstrate the current development status of PISSG technology.

Despite the current exciting achievements, ongoing research endeavors are required to unlock the full potential of hydrogel-based evaporators for practical applications in the near future. The focus of these efforts could be directed to the following aspects:

1) The mechanism of evaporation enthalpy: Although significant progress has been made in reducing evaporation enthalpy in recent years, the underlying mechanisms remain incompletely understood. There is a need to expand upon these aspects for in-depth exploration: 1) Mechanisms at the molecular level. Molecular dynamics simulations and infrared spectroscopy provide deeper insights into the interactions between water molecules and material surfaces. Moreover, the combined use of cryo-electron microscopy and high-speed atomic force microscopy enables in situ capture of the dynamic structure of evaporative interfacial water molecules at the sub-nanometer scale, such as the process of hydrogen bond network breaking, helping to figure out how these interactions influence the reduction of evaporation enthalpy; 2) Material Design. The regulation of interfacial water structure focuses on the precise control of hydrogen bond networks and the arrangement of interfacial water to further reduce enthalpy. This can be achieved through the design of hydrogen bond networks and strategies for controlling hydrophilic and hydrophobic micro-areas; 3) Multiscale synergistic effects. The reduction of evaporation enthalpy may involve the synergistic effects of multiple mechanisms, including thermal localization, enhanced water transport, and reduced interfacial energy. Future studies need to systematically analyze the interactions of these factors from a multiscale perspective to establish a more comprehensive theoretical model; and 4) Deep integration of experiment and theory. Combining experimental research with theoretical calculations enables more accurate prediction and validation of the

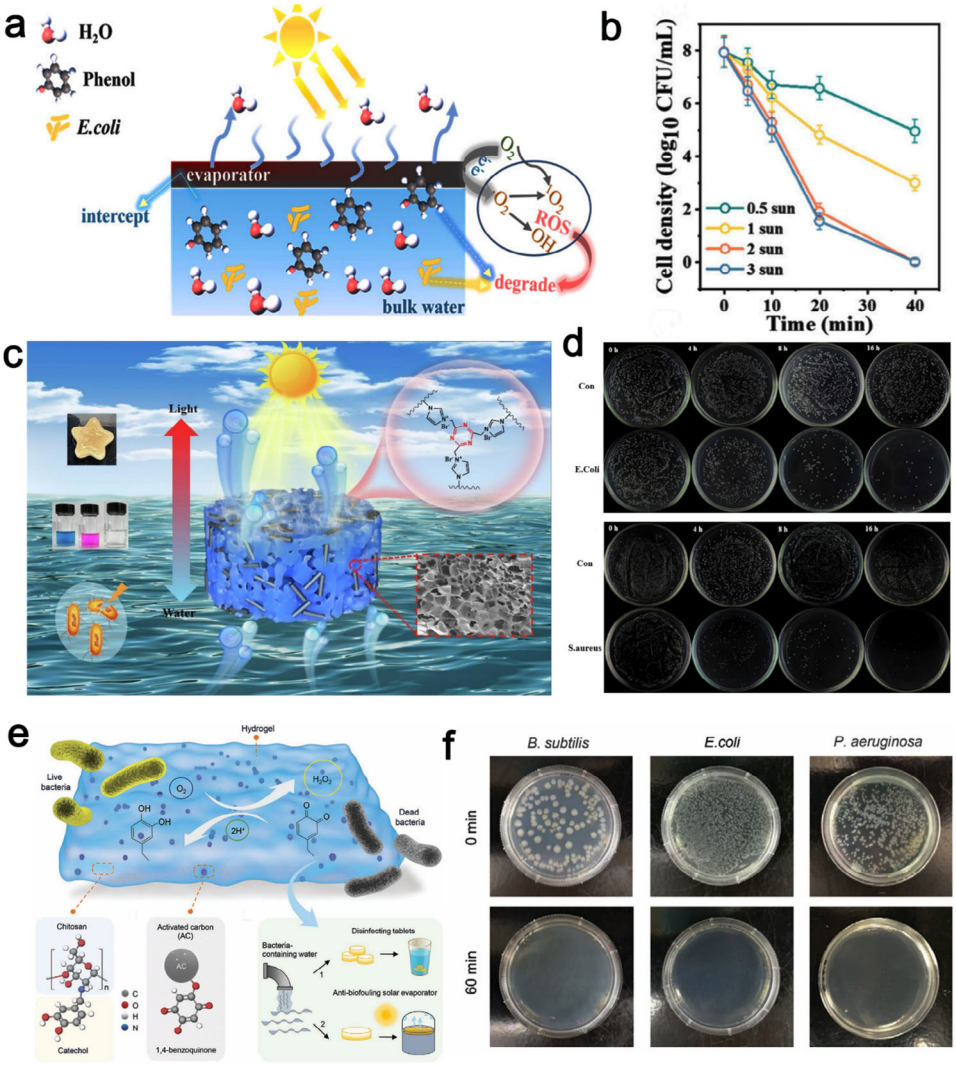


**Figure 21.** a) Schematic diagram of solar-driven *E. coli* elimination by an SA/CCC/$Cu^{2+}$ evaporator. b) Inactivation effect of *E. coli* of the SA/CCC/$Cu^{2+}$ evaporator under different sunlight intensities. Reproduced with permission.[143] Copyright 2024, The American Chemical Society. c) Schematic diagram of solar-driven PDIH evaporator. d) Bacterial culture plates of *E. coli* and *staphylococcus aureus* under PDIH treatment at different times (0, 4, 8, and 16 h). Reproduced with permission.[123] Copyright 2025, Elsevier. e) Schematics of ABHs for water disinfection and purification. f) Agar plates show the bacterial inactivation performance at 0 and 60 min. Reproduced with permission.[144] Copyright 2021, Wiley-VCH.

**Table 5.** Summary of recent hydrogel evaporators on sterilization.

| Evaporators | Bacterial species | Efficiency [1 h] | Refs. |
|---|---|---|---|
| SA/CCC/$Cu^{2+}$ | *E. coli* | 100% (40 min) | [143] |
| Au@ZIF-8/$Ti_3C_2T_x$/SA | *E. coli* | 99.54% | [145] |
| | *Staphylococcus aureus* | 97.22% | |
| AgMXene@Chitosan hydrogel | *E. coli* | 99.76% (15 min) | [146] |
| | *Staphylococcus aureus* | 99.41% (15 min) | |
| PDIH | *E. coli* | 95.54% (16 h) | [123] |
| | *Staphylococcus aureus* | 98.21% (16 h) | |
| ABHs | *B. subtilis* | 99.99% | [144] |
| | *E. coli* | | |
| | *P. aeruginosa* | | |

mechanisms behind evaporation enthalpy reduction, thereby guiding material design and performance optimization. Specifically, the hydrogen bond lifetime distribution can be determined through 3D infrared spectroscopy and compared with molecular dynamics simulation results. The evaporation enthalpy of microstructured samples can be directly measured using a nanocalorimeter to calibrate theoretical models. Additionally, X-ray absorption spectroscopy verifies the coordination state of interfacial water molecules, which corresponds with the electronic structure calculated by DFT.

2) Long-term stability and large-scale fabrication: Hydrogel-based evaporators, owing to their inherent salt-resistant properties, are capable of achieving stable water production over extended periods. However, to enhance the stability and durability of evaporators for deployment in diverse water sources (such as lakes, seas, brackish aquifers, rivers, and swamps), as well as under severe conditions (highly concentrated saline, acidic, and basic environments), more advanced designs incorporating antifouling coatings, self-healing polymers, and mechanically robust structures are essential. Additionally, developing affordable methods for large-scale solar evaporator production is essential to unlock the full capabilities of hydrogels. Key methods include replacing expensive polymer matrices and light-absorbing components with economical alternatives (for example, using cost-effective photothermal materials such as CuO, $MoS_2$, and carbon-based materials instead of high-cost precious metals), while also utilizing emerging 3D printing technology to facilitate efficient, large-scale hydrogel manufacturing. Simultaneously, improving collection efficiency, such as through the design of efficient water condensation systems, is equally critical for the optimization of hydrogel-based evaporators.
3) Exploration of new applications: Hydrogel-based evaporators have demonstrated their flexibility and environmental friendliness compared to other materials. The potential of hydrogel has not yet been fully exploited. While the currently studied applications need further optimization and extension, it is worth exploring innovative avenues to broaden the scope of hydrogel and drive the advancement of its cross-disciplinary applications.

## Acknowledgements

This work was supported by the National Natural Science Foundation of China (52161145409, 21976116), SAFEA of China ("Belt and Road" Innovative Talent Exchange Foreign Expert Project # 2023041004L) (High-end Foreign Expert Project # G2023041021L), and Alexander-von-Humboldt Foundation of Germany (Group-Linkage Program).

## Conflict of Interest

The authors declare no conflict of interest.

## Keywords

hydrogel, interfacial, photothermal, solar-driven, steam generation

[1] a) B. Yang, Z. Zhang, P. Liu, X. Fu, J. Wang, Y. Cao, R. Tang, X. Du, W. Chen, S. Li, H. Yan, Z. Li, X. Zhao, G. Qin, X. Chen, L. Zuo, *Nature* **2023**, *622*, 499; b) P. Tao, G. Ni, C. Song, W. Shang, J. Wu, J. Zhu, G. Chen, T. Deng, *Nat. Energy* **2018**, *3*, 1031.
[2] X. Wu, Y. Lu, X. Ren, P. Wu, D. Chu, X. Yang, H. Xu, *Adv. Mater.* **2024**, *36*, 2313090.
[3] Z. Yu, Y. Li, Y. Zhang, P. Xu, C. Lv, W. Li, B. Maryam, X. Liu, S. C. Tan, *Nat. Commun.* **2024**, *15*, 6081.
[4] L. Li, N. He, B. Jiang, K. Yu, Q. Zhang, H. Zhang, D. Tang, Y. Song, *Adv. Funct. Mater.* **2021**, *31*, 2104380.
[5] a) S. Alnajdi, A. Naderi Beni, A. A. Alsaati, M. Luhar, A. E. Childress, D. M. Warsinger, *Joule* **2024**, *8*, 3088; b) Y. Yao, P. Zhang, F. Sun, W. Zhang, M. Li, G. Sha, L. Teng, X. Wang, M. Huo, R. M. DuChanois, T. Cao, C. Boo, X. Zhang, M. Elimelech, *Science* **2024**, *384*, 333.
[6] M. Gao, L. Zhu, C. K. Peh, G. W. Ho, *Energy Environ. Sci.* **2019**, *12*, 841.
[7] a) Y. Qiu, Z. Zhou, C. Zhang, F. Jiang, Q. Zhang, J. Chen, *ACS Energy Lett.* **2022**, *7*, 3476; b) X. Li, T. Cooper, W. Xie, P. Hsu, *ACS Energy Lett.* **2021**, *6*, 2645; c) X. Wang, Z. Lin, J. Gao, Z. Xu, X. Li, N. Xu, J. Li, Y. Song, H. Fu, W. Zhao, S. Wang, B. Zhu, R. Wang, J. Zhu, *Nat. Water* **2023**, *1*, 391.
[8] S. Yu, Y. Gu, X. Chao, G. Huang, D. Shou, *J. Mater. Chem. A* **2023**, *11*, 5978.
[9] Y. Zheng, R. A. Caceres Gonzalez, K. B. Hatzell, M. C. Hatzell, *Joule* **2021**, *5*, 1971.
[10] a) H. Li, W. Zhang, J. Liu, M. Sun, L. Wang, L. Xu, *Adv. Funct. Mater.* **2023**, *33*, 2308492; b) L. Zhu, M. Gao, C. K. N. Peh, G. W. Ho, *Nano Energy* **2019**, *57*, 507.
[11] a) C. Onggowarsito, S. Mao, X. S. Zhang, A. Feng, H. Xu, Q. Fu, *Energy Environ. Sci.* **2024**, *17*, 2088; b) C. Lei, W. Guan, Y. Guo, W. Shi, Y. Wang, K. P. Johnston, G. Yu, *Angew. Chem., Int. Ed.* **2022**, *61*, 202208487.
[12] a) Y. Chen, Y. Zhu, Z. Wang, H. Yu, Z. Xiong, *ACS Appl. Mater. Interfaces* **2025**, *17*, 8158; b) J. Qiu, X. Xu, Z. Li, Y. Hu, G. Liu, X. Lv, J. Xu, B. Lu, *Nano Energy* **2024**, *130*, 110057.
[13] a) N. Chandra Adak, W. Lee, *Prog. Mater. Sci.* **2025**, *148*, 101377; b) X. Li, J. Li, L. Zou, M. Chen, H. Wang, L. Yang, R. Yang, H. Zhang, Y. Zhou, *Adv. Funct. Mater.* **2025**, 2504502.
[14] Z. Yu, R. Gu, Y. Tian, P. Xie, B. Jin, S. Cheng, *Adv. Funct. Mater.* **2022**, *32*, 2108586.
[15] a) E. G. Arafa, M. W. Sabaa, R. R. Mohamed, A. M. Elzanaty, O. F. Abdel-Gawad, *React. Funct. Polym.* **2022**, *174*, 105243; b) S. Kim, S. Jung, *Carbohyd. Polym.* **2020**, *250*, 116934.
[16] Q. Zhao, Y. Yang, B. Zhu, Z. Sha, H. Zhu, Z. Wu, F. Nawaz, Y. Wei, L. Luo, W. Que, *Desalination* **2023**, *568*, 116999.
[17] S. W. Sharshir, A. M. Algazzar, K. A. Elmaadawy, A. W. Kandeal, M. R. Elkadeem, T. Arunkumar, J. Zang, N. Yang, *Desalination* **2020**, *491*, 114564.
[18] X. Zhou, Y. Guo, F. Zhao, G. Yu, *Acc. Chem. Res.* **2019**, *52*, 3244.
[19] L. Shu, X. Zhang, Z. Wang, J. Liu, J. Yao, *Carbohyd. Polym.* **2024**, *327*, 121695.
[20] M. Li, M. Yang, B. Liu, H. Guo, H. Wang, X. Li, L. Wang, T. D. James, *Chem. Eng. J.* **2022**, *431*, 134245.
[21] G. Li, J. Xu, C. Xu, X. Xie, W. Chen, Y. Liu, *Chem. Eng. J.* **2024**, *486*, 150398.
[22] X. Lin, P. Wang, R. Hong, X. Zhu, Y. Liu, X. Pan, X. Qiu, Y. Qin, *Adv. Funct. Mater.* **2022**, *32*, 2209262.
[23] J. Chen, Y. Xie, M. Tian, J. Tian, Z. Liang, H. Xie, M. Lv, *Carbohyd. Polym.* **2025**, *356*, 123385.
[24] J. Yuan, X. Lei, C. Yi, H. Jiang, F. Liu, G. J. Cheng, *Chem. Eng. J.* **2022**, *430*, 132765.
[25] B. K. Sahu, B. C. Pattnayak, S. Mohapatra, *Desalination* **2024**, *581*, 117611.

[26] N. Hu, Y. Xu, Z. Liu, M. Liu, X. Shao, J. Wang, *Carbohyd. Polym.* **2020**, *243*, 116480.
[27] J. Gu, Z. Luan, X. Zhang, H. Wang, X. Cai, W. Zhan, X. Ji, J. Liang, *Mater. Horiz.* **2025**.
[28] X. Xu, Q. Zhao, Q. Liu, J. Qiu, J. Li, W. Zheng, J. Cao, L. Wang, W. Wang, S. Yuan, A. Fu, H. Yang, C. Wang, J. Xu, B. Lu, *Desalination* **2024**, *577*, 117400.
[29] M. Tan, J. Wang, W. Song, J. Fang, X. Zhang, *J. Mater. Chem. A* **2019**, *7*, 1244.
[30] Y. Zheng, R. Huang, Y. Yu, X. Wei, J. Yin, S. Zhang, *Water Res.* **2024**, *257*, 121707.
[31] M. Yang, Y. Wu, M. Chen, Y. Wang, L. Zhang, Y. Deng, D. Ye, Y. Zhan, G. Xiao, X. Jiang, *Small* **2024**, *20*, 2402151.
[32] F. Yang, Z. Bao, Z. Liang, G. He, J. Li, Q. Liang, J. Li, S. Luo, Y. Liu, *Chem. Eng. J.* **2024**, *490*, 151815.
[33] B. C. pattnayak, S. Mohapatra, *Desalination* **2025**, *604*, 118703.
[34] J. Wang, X. Li, Q. Wang, Q. Xu, Y. Wang, Z. Guo, X. Chen, *Sep. Purif. Technol.* **2025**, *361*, 131660.
[35] S. Qi, T. Jia, Y. Zhang, Y. Zhao, Y. Xing, M. Zhang, F. Wang, C. Chen, W.-Y. Wong, *Adv. Funct. Mater.* **2025**, 2503234.
[36] J. Zhao, A. Chu, J. Chen, P. Qiao, J. Fang, Z. Yang, Z. Duan, H. Li, *Chem. Eng. J.* **2024**, *485*, 150118.
[37] C. Fu, L. Liu, C. Xu, P. Tao, Y. Yang, L. Lu, Z. Zeng, T. Ren, *Adv. Funct. Mater.* **2024**, *34*, 2410616.
[38] B. Wang, H. Zhu, B. Shutes, *Nano Today* **2024**, *57*, 102370.
[39] Y. Jiang, Y. Gong, C. Guo, X. Xiang, *Desalination* **2025**, *608*, 118840.
[40] C. Song, M. S. Irshad, Z. Li, J. Hu, G. Shao, W. Liu, X. Xu, *Chem. Eng. J.* **2023**, *478*, 146566.
[41] J. He, Y. Fan, C. Xiao, F. Liu, H. Sun, Z. Zhu, W. Liang, A. Li, *Compos. Sci. Technol.* **2021**, *204*, 108633.
[42] H. Li, G. Tong, A. Chu, J. Chen, H. Yang, J. Fang, Z. Yang, H. Liu, L. Dong, *Nano Energy* **2024**, *124*, 109475.
[43] H. W. Lim, S. H. Park, S. J. Lee, *Desalination* **2023**, *550*, 116368.
[44] Q. Zhao, Z. Wu, X. Xu, R. Yang, H. Ma, Q. Xu, K. Zhang, M. Zhang, J. Xu, B. Lu, *Sep. Purif. Technol.* **2022**, *300*, 121889.
[45] H. Wan, X. Fu, Y. Chen, L. Zhao, T. Wang, Y. Liu, *Sep. Purif. Technol.* **2025**, *359*, 130795.
[46] X. Zhang, L. Sun, X. Wang, S. Zou, C. Cao, J. Hou, F. Guo, C. Li, W. Shi, *Chem. Eng. J.* **2024**, *497*, 154793.
[47] T. Wang, M. Li, H. Xu, X. Wang, M. Jia, X. Hou, S. Gao, Q. Liu, Q. Yang, M. Tian, L. Qu, Z. Song, X. Wu, L. Wang, X. Zhang, *Nano-Micro Lett.* **2024**, *16*, 220.
[48] Z. Zhang, Y. Luo, M. Li, B. Ge, L. Zhao, T. Zhang, G. Ren, Z. Zhang, *Chem. Eng. J.* **2024**, *488*, 151038.
[49] J. Wang, X. Liu, K. Zhang, *Chem. Eng. J.* **2025**, *514*, 163093.
[50] T. Zhang, J. Yang, Y. Yang, C. Li, X. Xu, Z.-Z. Yu, X. Li, *Desalination* **2025**, *602*, 118599.
[51] Y. Liu, Z. Zhang, J. Wang, C. Hu, J. Tang, M. Shi, H. Cui, D. Qi, *Chem. Eng. J.* **2025**, *513*, 162853.
[52] J. Jin, C. Wang, D. Wei, B. Wang, X. Lin, W. Zhang, C. Shi, Z. Zhao, L. Wang, F. Wang, *Small* **2025**, *21*, 2411624.
[53] S. Mallakpour, M. Tukhani, C. M. Hussain, *Adv. Colloid. Interfac.* **2021**, *292*, 102415.
[54] Z. Wang, X. Zhang, L. Shu, J. Yao, *Carbohyd. Polym.* **2023**, *319*, 121161.
[55] H. Zou, X. Meng, X. Zhao, J. Qiu, *Adv. Mater.* **2023**, *35*, 2207262.
[56] a) J. Ren, G. Chen, H. Yang, J. Zheng, S. Li, C. Zhu, H. Yang, J. Fu, *Adv. Mater.* **2024**, *36*, 2412162; b) D. Kong, Z. M. El-Bahy, H. Algadi, T. Li, S. M. El-Bahy, M. A. Nassan, J. Li, A. A. Faheim, A. Li, C. Xu, M. Huang, D. Cui, H. Wei, *Adv. Compos. Hybrid. Ma.* **2022**, *5*, 1976.
[57] X. Zhou, F. Zhao, Y. Guo, Y. Zhang, G. Yu, *Energ. Environ. Sci.* **2018**, *11*, 1985.
[58] Y. Guo, H. Lu, F. Zhao, X. Zhou, W. Shi, G. Yu, *Adv. Mater.* **2020**, *32*, 1907061.
[59] W. Li, J. Li, L. Ding, X. Zhu, R. Sun, K. Chang, *Adv. Funct. Mater.* **2024**, *34*, 2411387.
[60] X. Xu, Q. Liu, J. Qiu, Q. Zhao, S. Yuan, H. Li, Z. Li, A. Fu, J. Xu, B. Lu, *Desalination* **2025**, *597*, 118364.
[61] R. Zhao, X. Chen, X. Chen, P. Zhang, C. Luo, P. Zhang, M. Chao, L. Yan, *J. Mater. Chem. A* **2025**, *13*, 5684.
[62] T. Yang, X. Mu, J. Zhou, P. Wang, H. Chen, X. Wang, L. Miao, *Sol. Rrl.* **2022**, *6*, 2200586.
[63] X. Yu, J. Fang, X. Kong, Z. Yu, S. Zheng, C. Pan, H. Liang, L. Wang, H. Yu, Z. Liu, L. Fan, Q. Zuo, X. Wu, F. Gan, Z. Li, C.-w. Kan, J. Yan, X. Wang, *Chem. Eng. J.* **2025**, *505*, 159893.
[64] M. Yang, L. Zhang, D. Ye, Y. Dong, Y. Zhan, X. Jiang, *Chem. Eng. J.* **2024**, *480*, 148226.
[65] J. Xu, G. Wang, L. Zhu, G. Jiang, Y. Lei, Z. Zeng, L. Xue, *Chem. Eng. J.* **2023**, *455*, 140704.
[66] J. Ma, X. Sun, Y. liu, L. Wang, M. An, M. Kim, Y. Yamauchi, N. Khaorapapong, Z. Yuan, *Nano Energy* **2025**, *137*, 110781.
[67] a) Z. Zhang, X. Li, G. Liu, S. Qi, J. Lv, B. Ge, T. Zhang, G. Ren, Z. Zhang, *Desalination* **2025**, *606*, 118767; b) Q. Zhu, M. Liu, Y. Li, G. Feng, Z. Xu, L. Geng, X. Yu, *Sep. Purif. Technol.* **2025**, *368*, 133033; c) L. Zheng, Y. Peng, Y. Shao, Y. Sun, M. Salimi, M. Amidpour, N. Yu, Z. Chen, *Sep. Purif. Technol.* **2025**, *363*, 132009.
[68] J. Lee, K. Kim, S. Park, G. Y. Yoon, J. Kim, S. J. Lee, *Nano Energy* **2020**, *77*, 105130.
[69] Y. Guo, L. S. de Vasconcelos, N. Manohar, J. Geng, K. P. Johnston, G. Yu, *Angew. Chem., Int. Ed.* **2022**, *61*, 202114074.
[70] G. Ma, X. Qi, Q. Wei, X. Shi, Y. Chang, Y. Guo, Z. Hu, X. Ma, *Green Chem.* **2024**, *26*, 4749.
[71] X. Xu, N. Guillomaitre, K. S. S. Christie, R. K. n. Bay, N. Bizmark, S. S. Datta, Z. J. Ren, R. D. Priestley, *ACS Central Sci.* **2023**, *9*, 177.
[72] C. Hu, J. Liu, C. Li, M. Zhao, J. Wu, Z.-Z. Yu, X. Li, *ACS Appl. Mater. Interfaces* **2024**, *16*, 13060.
[73] C. Li, S. Cao, J. Lutzki, J. Yang, T. Konegger, F. Kleitz, A. Thomas, *J. Am. Chem. Soc.* **2022**, *144*, 3083.
[74] W. Li, Y. Wei, H. Zeng, Z. Huang, J. Wu, S. Yu, *Energ. Convers. Manage.* **2024**, *315*, 118777.
[75] H. M. Wilson, H. W. Lim, S. J. Lee, *ACS Appl. Mater. Interfaces* **2022**, *14*, 47800.
[76] Y. Peng, S. Tang, X. Wang, R. Ran, *Macromol. Mater. Eng.* **2021**, *306*, 2100309.
[77] Z. Lei, X. Sun, S. Zhu, K. Dong, X. Liu, L. Wang, X. Zhang, L. Qu, X. Zhang, *Nano-Micro Lett.* **2021**, *14*, 10.
[78] Y. Lu, D. Fan, Y. Wang, H. Xu, C. Lu, X. Yang, *ACS Nano* **2021**, *15*, 10366.
[79] Y. Guo, F. Zhao, X. Zhou, Z. Chen, G. Yu, *Nano Lett.* **2019**, *19*, 2530.
[80] G. Yang, Z. Yin, X. Han, Z. Hong, C. Xie, Y. Ma, J. Xu, M. Xue, *Chem. Eng. J.* **2025**, *512*, 162459.
[81] X. Su, D. Hao, M. Sun, T. Wei, D. Xu, X. Ai, X. Guo, T. Zhao, L. Jiang, *Adv. Funct. Mater.* **2022**, *32*, 2108135.
[82] S. Yu, Y. Wei, D. Fang, W. Li, J. Yu, Y. Tang, J. Bai, J. Wu, *Desalination* **2024**, *586*, 117909.
[83] H. Mo, Y. Wang, *Water Res.* **2022**, *226*, 119276.
[84] S. Zhang, M. Li, C. Jiang, D. Zhu, Z. Zhang, *Adv. Sci.* **2024**, *11*, 2308665.
[85] J. Gu, Y. Zhang, P. Xiao, Q. Fan, J. Guan, K. Liang, T. Chen, *Chem. Eng. J.* **2024**, *490*, 151550.
[86] R. Yang, L. Xia, C. Tan, F. Liu, F. Guo, X. Zhang, Y. Yu, *Chem. Eng. J.* **2024**, *481*, 148671.
[87] Z. Sun, C. Han, S. Gao, Z. Li, M. Jing, H. Yu, Z. Wang, *Nat. Commun.* **2022**, *13*, 5077.
[88] H. Zhang, X. Li, X. Liu, Y. Du, W. Xie, S. Zheng, L. Yang, J. Shi, D. Jing, *Chem. Eng. J.* **2023**, *473*, 145484.
[89] L. Zhang, Y. Zhang, M. Zou, C. Yu, C. Li, C. Gao, Z. Dong, L. Wu, Y. Song, *Adv. Funct. Mater.* **2023**, *33*, 2300318.

[90] X. Geng, P. Yang, Y. Wan, *Nano Energy* **2024**, *123*, 109434.
[91] D. Liang, J. Tang, Q. Sun, W. Zhao, J. Li, Y. Liu, Z. Liu, X. Yang, H. Liu, G. Xue, *Carbohyd. Polym.* **2025**, *353*, 123302.
[92] F. Zhao, X. Zhou, Y. Shi, X. Qian, M. Alexander, X. Zhao, S. Mendez, R. Yang, L. Qu, G. Yu, *Nature Nanotech.* **2018**, *13*, 489.
[93] X. Wang, Z. Ma, S. Xu, D. Zheng, B. Bai, S. Zong, *Water Res.* **2025**, *268*, 122709.
[94] a) D. He, G. Huang, Z. Zhou, Q. Hu, J. Ding, J. Wu, M. Li, X. Ruan, X. Jiao, Y. Xie, *Adv. Funct. Mater.* **2024**, 2419801; b) Y. Cui, X. Liang, J. Wang, N. Kumar, J. Sun, C. Wang, *J. Energy Chem.* **2025**, *103*, 888.
[95] X. Liang, T. Gao, Y. Cui, Q. Dong, X. Li, A. Labidi, E. Lichtfouse, F. Li, F. Yu, C. Wang, *Appl. Catal. B-Environ.* **2024**, *357*, 124326.
[96] a) Y. Li, P. Liu, Y. Gao, Y. Feng, P. Li, X. Chen, *J. Energy Chem.* **2024**, *95*, 208; b) M. Gao, T. Zhang, S. W. L. Ng, W. Lu, G. Tian, W. L. Ong, S. M. Kozlov, G. W. Ho, *Adv. Energy Mater.* **2025**, 2404198.
[97] a) H. Li, Y. Tang, W. Yan, M. Liu, Z. Wang, J. Li, F. Yu, *Appl. Catal. B-Environ.* **2024**, *357*, 124346; b) J. Wang, Y. Li, L. Deng, N. Wei, Y. Weng, S. Dong, D. Qi, J. Qiu, X. Chen, T. Wu, *Adv. Mater.* **2017**, *29*, 1603730.
[98] A. Agrawal, S. H. Cho, O. Zandi, S. Ghosh, R. W. Johns, D. J. Milliron, *Chem. Rev.* **2018**, *118*, 3121.
[99] Y. Li, Y. Shi, H. Wang, T. Liu, X. Zheng, S. Gao, J. Lu, *Carbon Energy* **2023**, *5*, 331.
[100] W. He, L. Zhou, M. Wang, Y. Cao, X. Chen, X. Hou, *Sci. Bull.* **2021**, *66*, 1472.
[101] Y. Wei, W. Li, S. Zhang, J. Yu, Y. Tang, J. Wu, S. Yu, *Adv. Funct. Mater.* **2024**, *34*, 2401149.
[102] Y. Zhang, Y. Wang, B. Yu, K. Yin, Z. Zhang, *Adv. Mater.* **2022**, *34*, 2200108.
[103] R. Takahata, S. Yamazoe, K. Koyasu, K. Imura, T. Tsukuda, *J. Am. Chem. Soc.* **2018**, *140*, 6640.
[104] J. Wu, F. Yan, J. Zhao, L. Qian, T. Cheng, J. Su, L. Bi, Y. Huang, W. Wang, Z. Zhang, F. Luo, S. Ning, *Adv. Funct. Mater.* **2024**, *34*, 2411358.
[105] H. Ma, C. Zhao, G. Chen, Y. Dong, *Nat. Commun.* **2019**, *10*, 3368.
[106] L. Tian, L. Han, F. Wang, H. Shen, Q. Li, L. Zhu, S. Chen, *Adv. Energy Mater.* **2024**, *15*, 2404117.
[107] X. Li, R. Yang, L. Zou, S. Zheng, M. Chen, J. Wen, H. Zhang, C. Wu, Y. Zhang, Y. Zhou, *Adv. Mater.* **2025**, *37*, 2416283.
[108] M. Chen, S. Li, S. Guo, H. Yan, S. C. Tan, *Green. Energy. Environ.* **2024**, *9*, 1812.
[109] N. He, Y. Yang, H. Wang, F. Li, B. Jiang, D. Tang, L. Li, *Adv. Mater.* **2023**, *35*, 2300189.
[110] T. Heinze, N. Pastore, *Nat. Commun.* **2023**, *14*, 362.
[111] Y. Wang, X. Wu, X. Yang, G. Owens, H. Xu, *Nano Energy* **2020**, *78*, 105269.
[112] X. Wu, Z. Wu, Y. Wang, T. Gao, Q. Li, H. Xu, *Adv. Sci.* **2021**, *8*, 2002501.
[113] L. Zhang, Q. Zhuang, Z. Wen, P. Zhang, W. Ma, Q. Wu, H. Yun, *Adv. Colloid Interfac.* **2021**, *294*, 102465.
[114] Y. Wang, W. Zhao, Y. Lee, Y. Li, Z. Wang, K. C. Tam, *Nat. Commun.* **2024**, *15*, 6157.
[115] K. Chang, Y. Li, Y.-A.-M. Xi, J. Xu, Y. Zhang, *Nano Energy* **2024**, *132*, 110369.
[116] A. Peters, S. C. Iden, W. Durner, *Vadose Zone J.* **2019**, *18*, 190064.
[117] Q. Chen, H. Zhang, L. Zou, R. Yang, G. Zeng, P. Lin, L. Yang, M. Zheng, X. Li, *Chem. Eng. J.* **2025**, *506*, 160061.
[118] H. Guo, P. Yan, X. Sun, J. Song, F. Zhu, X. Guan, S. W. Sharshir, J. Shi, Z. Li, X. Xu, M. An, *Chem. Eng. J.* **2024**, *485*, 149918.
[119] H. Zhang, P. Tang, K. Yang, Q. Wang, W. Feng, Y. Tang, *Desalination* **2023**, *558*, 116620.
[120] L. Yan, X. Yang, H. Zeng, Y. Zhao, Y. Li, X. He, J. Ma, L. Shao, *J. Membrane Sci.* **2023**, *668*, 121243.
[121] C. Fu, G. Tian, S. He, L. Yao, Z. Guo, *ACS Appl. Mater. Interfaces* **2024**, *16*, 37757.
[122] S. Gao, J. Chen, Y. Zheng, A. Wang, D. Dong, Y. Zhu, Y. Zhang, W. Fang, J. Jin, *Adv. Funct. Mater.* **2022**, *32*, 2205990.
[123] X. He, R. Cao, J. Li, Z. Wang, Y. Liang, P. Ma, S. Ma, X. Tian, Y. Lu, Z. Wang, X. Lu, *Desalination* **2025**, *604*, 118689.
[124] Y. Lu, Z. Li, J. Liang, X. Xu, G. Zhang, H. Min, *Desalination* **2024**, *592*, 118196.
[125] R. Niu, Y. Ding, L. Hao, J. Ren, J. Gong, J. Qu, *ACS Appl. Mater. Interfaces* **2022**, *14*, 45533.
[126] X. Gao, L. Sun, P. Hao, S. Zhang, Y. Shen, J. Hou, F. Guo, C. Li, W. Shi, *Sep. Purif. Technol.* **2025**, *355*, 129615.
[127] L. Shu, X.-F. Zhang, S. Yang, J. Qiu, J. Yao, *Sep. Purif. Technol.* **2024**, *334*, 125971.
[128] X.-P. Li, C. Hu, X. Yan, L. Li, Z. Ming, H. Yao, Y. Zhao, H. Li, X. Li, *Sep. Purif. Technol.* **2025**, *358*, 130260.
[129] Z.-Y. Wang, L. Xu, C.-H. Liu, S.-J. Han, M.-L. Fu, B. Yuan, *J. Mater. Chem. A* **2024**, *12*, 10991.
[130] Z. Zhu, T. Wang, S. Ren, Y. Feng, Y. Zhang, S. Qian, W. Tang, X. Yin, T. Wu, S. Gao, *Desalination* **2025**, *606*, 118758.
[131] S. Pu, Y. Liao, K. Chen, J. Fu, S. Zhang, L. Ge, G. Conta, S. Bouzarif, T. Cheng, X. Hu, K. Liu, J. Chen, *Nano Lett.* **2020**, *20*, 3791.
[132] H. Wang, W. Xie, B. Yu, B. Qi, R. Liu, X. Zhuang, S. Liu, P. Liu, J. Duan, J. Zhou, *Adv. Energy Mater.* **2021**, *11*, 2100481.
[133] Z. Huang, C. Li, W. Ying, N. Pan, X. Lei, J. Zhang, R. Wang, J. Wang, *Nano Energy* **2024**, *126*, 109673.
[134] J. Sun, Y. Liu, J. Wei, P. Wei, T. Chen, *Chem. Eng. J.* **2024**, *485*, 149836.
[135] X. Jing, L. Chen, Y. Li, H. Yin, J. Chen, M. Su, F. Liu, T. Abdiryim, F. Xu, J. You, X. Liu, *Small* **2024**, *20*, 2405587.
[136] G. Li, W. Ma, J. Zhou, C. Wu, C. Yao, H. Zeng, J. Wang, *Chinese Chem. Lett.* **2025**, *36*, 110449.
[137] C. Wan, Z. Li, X. Yang, Y. Yang, X. Li, Y. Gao, L. Wang, W. Lü, *J. Colloid Interf. Sci.* **2025**, *687*, 376.
[138] K.-T. Huang, W.-H. Hung, Y.-C. Su, F.-C. Tang, L. D. Linh, C.-J. Huang, L.-H. Yeh, *Adv. Funct. Mater.* **2023**, *33*, 2211316.
[139] Y. Wang, H. Jiang, Y. Zhang, Z. Song, Z. Chen, K. Sui, W. Fan, P. Qi, *Chem. Eng. J.* **2024**, *481*, 148512.
[140] E. Kim, X. Ma, J. Zhou, J. Gao, A. Liu, Y. Ru, Y. Kim, S. Lee, D.-M. Shin, *Adv. Funct. Mater.* **2025**, 2419710.
[141] Z. Gong, A. Suwardi, J. Cao, *Adv. Funct. Mater.* **2025**, 2423371.
[142] Z. Zhang, T. Zhou, X.-Y. Kong, Y. Wu, W. Xin, Y. Cui, L. Yang, T. Li, X. Li, Q. Wang, W. Chen, L. Jiang, L. Wen, *Nano Res.* **2023**, *16*, 11288.
[143] N. An, M. Ma, Y. Chen, Z. Wang, Q. Li, *ACS Est. Eng.* **2025**, *5*, 732.
[144] Y. Guo, C. M. Dundas, X. Zhou, K. P. Johnston, G. Yu, *Adv. Mater.* **2021**, *33*, 2102994.
[145] Z. Fang, Y. Liu, J. Qi, M. Yu, Y. Wang, Y. Qiu, Z. Ma, S. Liu, *Mater. Today Chem.* **2025**, *43*, 102467.
[146] S. Hao, X. Chen, T. Zhao, Y. Jiang, W. Wang, B. Pan, J. Liu, L. Dong, F. Wang, *ACS Appl. Energy Mater.* **2024**, *7*, 1250.

**Yongqian Cui** received her master degree from Heilongjiang University in 2022. Currently she is a Ph.D. candidate in the School of Environmental Science and Engineering, Shaanxi University of Science and Technology under the supervision of Prof. Chuanyi Wang. Her present research interest focuses on the design of hydrogel-based evaporators for extraordinary water purification.

**Chuanyi Wang** FRSC, is a distinguished professor at Shaanxi University of Science & Technology (SUST), China. Before moving to SUST in 2017, he was a distinguished professor of Chinese Academy of Sciences (CAS, 2010–2017). He obtained his Ph.D. degree from Institute of Photographic Chemistry of CAS in 1998, worked in Germany as an Alexander von Humboldt research fellow from 1999 to 2000, and then worked in USA from 2000 to 2010. Currently, Dr. Wang also serves as an associate editor or editorial board member for number of international journals. His research interest covers eco-materials, energy conversion and environmental photocatalysis.